Second Deliverable to

The FERMI @ Elettra
Technical Optimization Study

entitled:

"General Layout and Parameters and Physics Studies of Longitudinal Space Charge, the Spreader, the Injector, and Preliminary FEL Performance"

submitted by:

Lawrence Berkeley National Laboratory
1 Cyclotron Road
Berkeley, CA 94720

John Byrd
John Corlett
Larry Doolittle
William Fawley
Steven Lidia
Gregory Penn
Alex Ratti
John Staples
Russell Wilcox
Jonathan Wurtele
Alexander Zholents

September 1, 2005

This report constitutes the second deliverable of LBNL's contracted role in the FERMI @ Elettra Technical Optimization study. It describes the general layout and systems parameters of the facility, and details physics studies of longitudinal space charge, the beam spreader region, injector studies, and preliminary FEL studies using input from start-to-end simulations.

Conceptual design of FERMI @ Elettra

Overview of the facility

The FERMI @ Elettra facility will make use of the existing GeV linac at Sincrotrone Elettra, which will become available for dedicated FEL applications following the completion of construction of a new injector booster complex for the storage ring. With a new rf photocathode injector, and some additional accelerating sections, this linac will be capable of providing high brightness bunches at 1.2 GeV and up to 50 Hz repetition rates. Figure 1 shows a preliminary CAD drawing of the proposed facility, with the linac-based FEL facility adjacent to the Elettra storage ring building.

To accommodate the new rf photocathode gun, the tunnel which houses the existing linac and thermionic gun will be extended upstream. This will be a relatively minor investment in additional excavation and will take advantage of the present roadway cutting, already at the level of the linac and extending backward several meters.

An S-band rf photocathode gun, with spatial and temporal control of the photocathode laser system, will provide high brightness electron bunches at up to 50 Hz rate. Flexibility in bunch parameters will be incorporated into the systems design. Accelerating sections raise the beam energy to ~100 MeV at the exit of the injector.

A laser heater system following the injector system will provide control of the uncorrelated energy spread in the beam and minimize potential impact of the microbunching instability. The laser heater also allows opportunity for implementing useful diagnostics systems.

Two magnetic bunch compressors are planned, inserted at 230 MeV and at 650 MeV. The final energy of the beam, 1.2 GeV, is determined by the accelerator section maximum gradient, available RF power including overhead and de-rating for reliable operations, and off-crest operation for control of energy chirp.

The linac is installed in a tunnel about 5 m below ground level, and the new facility will include a transport line to take the beam up to an undulator hall at or near the surface. This vertical ramp allows inclusion of useful diagnostics, and is carefully designed to minimize perturbations to the beam quality.

In the undulator hall, the electron beam may be directed to the longer-wavelength FEL (FEL-I) by a transport line which introduces a horizontal offset to the beam, or to the short-wavelength FEL (FEL-II) in a direct line to avoid perturbation to beam quality due to CSR in bend magnets.

A timing system based on transmission of optical signals over a highly stabilized fiber optic system will distribute timing signals throughout the facility. This provides synchronization of the photocathode laser to the RF gun phase, stabilized drive signals to RF systems in the facility, and synchronization of the FEL seed laser with the arrival time of the electron beam.

The seeded FEL process occurs in one stage of harmonic generation for FEL-I, and in a two-stage cascade for FEL-II. For FEL-II, both a fresh-bunch approach and a whole-bunch seeding technique are being developed. The x-ray pulse duration is determined by the seed laser, and both short-pulse (~40-100 fs) and long pulse (~0.5-1.0 ps) schemes are under development.

The photon beams from the FELs are transported in beamlines to hutches an adjoining downstream experimental hall. The electron beams are dumped following the final radiating undulator. Laser systems in the experimental area are synchronized to the FEL output using the stabilized optical timing system distributed around the facility.

Figure 2 shows the machine layout with various sections identified; INJ – injector, L1-L4 – linac sections, BC1,2 - bunch compressors, MTC1,2 – matching section, RAMP – vertical transport line, SPRD – beam spreader section, FEL1,2 – FEL's.

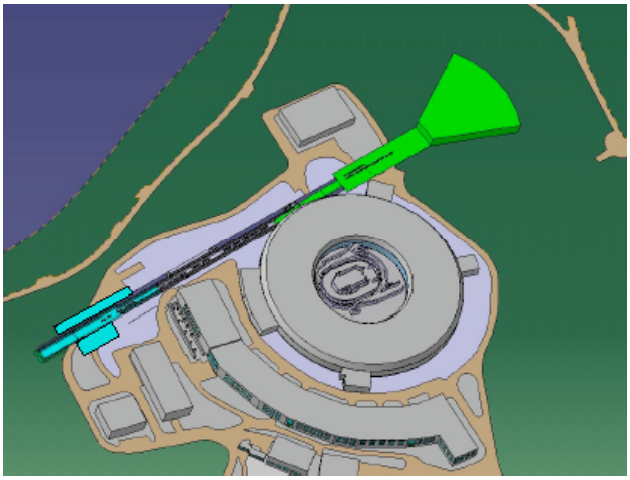

Figure 1: The FERMI FEL facility shown adjacent to Elettra.

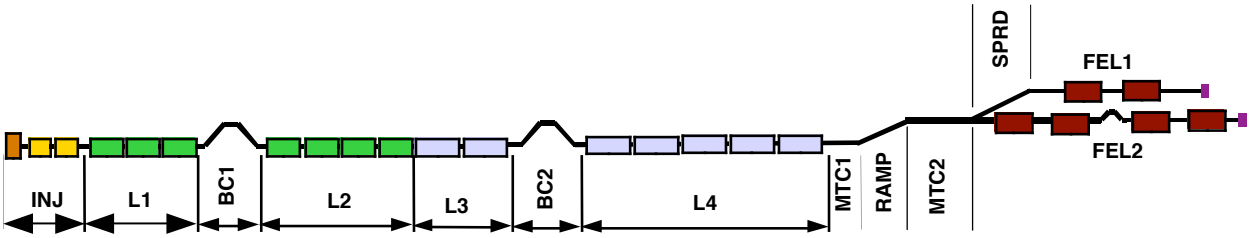

Figure 2: FERMI @ Elettra machine layout showing major section

Injector

The injector major systems are; photocathode laser, RF gun, booster linacs, emittance compensation solenoids, and laser heater. A diagnostics beamline will be incorporated in a branch line following the RF gun, to allow analysis of the beam phase space at the exit of the gun. A high quality electron source is essential to meet the requirements for photon production in the FERMI @ Elettra FEL. Two different bunch charge regimes have been explored; low (few hundreds of pC) and high (~1nC). In the first case, the limited charge extracted from the photocathode allows production of a relatively short bunch and to compress it at higher energies down to a few hundreds of fs, attaining a high peak current bunch with a very low slice emittance. The second case is optimized for the possibility to produce a longer bunch required for the harmonic cascade (FEL-II). Details of the injector design are presented in [1].

Photocathode laser

The photocathode laser must produce up to 1 nC of charge, and requires UV pulses with energy in the few hundred μJ range to produce low thermal emittance from a copper cathode with quantum efficiency ~10^{-5}. Taking into account the losses associated with temporal and spatial shaping systems, the harmonic conversion, and the need of a relatively large bandwidth to support a pulse with <1 ps risetime, we choose a Ti:sapphire system with >15 mJ in the infrared.

Effects of intensity modulation of the laser in driving longitudinal space charge fluctuations are discussed in [2].

RF photocathode gun

The difference between 'European' S-band and 'U.S.' S-band frequencies makes it difficult to take an established S-band gun design and apply it directly to the FERMI @ Elettra project, however existing designs may be scaled to the required frequency. Operating at up to 50Hz pulse rate sets demands on the thermal control of the gun, however there are designs, such as the LCLS gun, that operate at similar high repetition rate. An attractive choice for the electron gun is the SLAC/BNL/UCLA 1.6 cell s-band gun III, based upon the demonstrated high performance of this design and its descendants. Gun design is discussed in more detail in [1].

Booster linac

Two sections of traveling wave structure provide ~100 MeV total energy to the beam in the injector. These sections work in $2/3\pi$ mode with on-axis coupling, have relatively weak wakefields, and have solenoidal windings for focusing. Effects of wakefields are discussed in [3,4].

Laser heater

At the end of the injector a "laser heater" is used to induce controlled rapid energy modulation in the bunch and effectively 'heat-up' the beam. A laser pulse interacts with the e-beam in a short undulator inserted in a chicane. The laser heater is required to provide Landau damping of microbunching instabilities in the beam, as described in [2,3]. The device will have a secondary and important function as an electron beam diagnostics tool, described in [5]. The required laser pulse peak power is moderate (below 10 MW in a pulse duration of a few ps) and infrared wavelength can be used, from the photoinjector laser or from the fiber-optic timing system master oscillator.

Main linac

Three types of accelerating sections are used in the linac, color-coded in Figure 2. Injector sections (see above) are yellow. Seven CERN-type sections (green color in Figure 2) are used before and after the first chicane. Like the injector sections, these are traveling wave (TW) structures operating in $2\pi/3$ mode and with on- axis coupling between cells. Seven Elettra-sections (blue color in Figure 2) form the high-energy portion of the linac. These final sections are backward traveling wave (BTW) structures that are coupled magnetically, operate in $3\pi/4$ mode, and provide high shunt impedance.

To meet the stringent requirements of the project the present RF systems will be completely revised and upgraded. Stabilized modulators and feedback around the RF stations will be employed to meet phase and amplitude stability requirements, and RF systems will be integrated with the stabilized timing system, as reported in [6].

Accelerating structures and wakefields

The magnetic coupling of the BTW structures demands a small iris radius compared to on-axis coupled structures, and for this reason the BTW structure wakefields are stronger than for the TW structures. We find both longitudinal and transverse wakefield effects are controllable, and a study of the emittance growth under the combined influence of the short-range transverse

wakefields, injection offset, initial emittance and misaligned accelerating sections is reported in [4]. Details of overall accelerator optimization studies ("start-to-end") are described in [3].

Bunch compressors

The bunch compression uses a 'standard' technique of two chicanes of rectangular dipoles. The off-crest acceleration of the electron beam in the linac sections generates a correlated energy spread which is used with the energy-path length correlation given by the chicanes' optics to provide a compression in bunch length. The beam length is compressed by a factor of between 8 and 11 depending on details of the operating mode, and flexibility to adjust each compressor is incorporated into the design. The main challenge in the design of the compressors is to minimize the interaction between the coherent synchrotron radiation (CSR) and the longitudinal space charge (LSC), since this is the cause of the microbunching instability and the main factor degrading the beam quality. A laser heater is installed in the injector to suppress the instability.

Vertical ramp

The lattice of the vertical ramp is designed such that the first two bending magnets and the last two bending magnets are separated by $-I$ transport matrixes in both x and y planes, *i.e* π betatron phase advance. A FODO lattice consisting of two doublets is used for this purpose. This constrains the dispersion function between the pairs of magnets and mitigates the emittance excitation due to CSR effects. The lattice in the middle section between magnet pairs is also a FODO structure, with π phase advance in both planes in the high-beta case and 3π phase advance in the low-beta case. The $-I$ transport matrix in the middle section is important for a compensation of the emittance excitation due to CSR effects.

FEL'S

The FEL configuration relies on a Low-Gain-Harmonic-Generation (LGHG) scheme, similar to HGHG [7,8]. In the LGHG configuration, the use of high radiation power in the modulator(s) produces micro-bunching in the low-gain regime (no self-modulation), and permits relatively short undulator lengths. Figure 3 shows the principle, as employed in FEL-I. The modulating undulators are of planar design, and only the final radiating undulator is an APPLE-type design to allow control of the output polarization.

In the case of FEL-II, a delay chicane is placed following the radiator of the first optical klystron. This ensures that a "virgin" electron-beam portion, whose electrons instantaneous energy spread has been not increased by FEL interaction in the upstream undulators, is brought into temporal synchronism with the radiation pulse. Simulations are reported in [9].

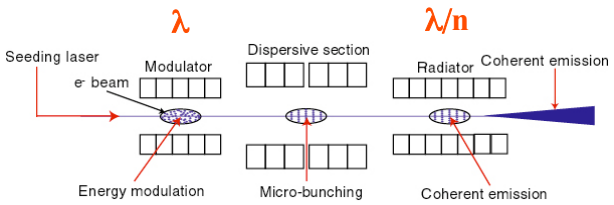

Figure 3: The principle of harmonic generation

FEL seed laser

The main requirement for this laser is to deliver sufficiently high peak power (~100 MW), at wavelengths tunable in the range 240-360 nm. Other parameters of the seed laser pulses are:

Gaussian profiles, pulse duration in the range 0.2- 1 ps, high stability of the pulse energy, high stability of the central wavelength, spot size 200-300 μm.

The requirement for such a broad UV tuning can be met by using parametric amplification in the visible or near infrared, followed by harmonic generation. In addition, the high UV pulse energy needed (100 μJ range with 1 ps pulses) imposes that the energy of the pulses that will pump the parametric amplifier should be ~15 mJ.

Timing and synchronization systems

The timing system will play a crucial role in achieving the expected performance of the FERMI @ Elettra FELs due to the sub-ps electron bunch length and the expanded use of fs-lasers as key components. The timing system intended for a user facility that is operated on a 24-h, 7-d basis, must be stable and reliable. The fundamental components of the system are an optical reference oscillator, the fiber optic stabilized links, and the local optical to electrical converters, needed for the RF plant synchronization. Using commercial 1550 nm components, jitter at the level of 10 fs is expected between remote laser systems. Concepts are discussed in [10,11,12].

Instrumentation

The successful implementation of FEL schemes calls for precise knowledge of electron beam properties. Measurements of each of its 6 phase space dimensions will be employed, including position and momentum in both transverse planes, beam energy, bunch length, and total charge. At a minimum the first and second moments in each dimension will be measured, the detailed electron distribution in each dimension as well as the correlations between dimensions. Electron beam diagnostics are reported in [13]. Methods to measure time-dependent beam quantities with sub-ps resolution are being investigated, including diagnostics in the laser heater [5].

Accelerator and FEL modeling

Design studies are in progress to model the FERMI @ Elettra FEL from start-to-end. Two operational scenarios are under development – for a short-pulse (40-100 fs) at the FEL and for a long-pulse (0.5-0.8 ps) at the FEL.

The injector systems have been modeled and optimized as reported in [1], and the output of the injector models is used as input for the rest of the machine. Optimization of all accelerator components downstream of the gun, aimed at achieving high peak current, low energy spread and low emittance electron beam necessary for the FEL, has been performed in simulations including effects of space charge, coherent synchrotron radiation, and wakefields as reported in [3]. Major parameters are shown in Table 1.

The longitudinal beam phase space is affected by nonlinearities from space charge at low energy, rf curvature, longitudinal wakefields and second order (chromatic) optics in the chicanes. The optimization process combines these effects in such a way to linearise as much as possible the longitudinal phase space. Very effective minimization of the emittance growth from transverse wakefields may be achieved by use of a pair of correctors in the linac. Simulations demonstrate the transverse wakefields are manageable, with negligible emittance growth after the corrections.

Using the electron beam properties determined by the accelerator optimization (start-to-end) studies, the FEL performance has been studied in simulations [9]. Free parameters are power of the input seed, the lengths of the individual modulator and radiator undulators, the strengths (i.e.

the R56's) of the dispersive sections, the choice of the actual harmonic numbers to reach a given wavelength. Major parameters are shown in Table 1.

Table 1. Major parameters for the FERMI @ Elettra FEL

Parameter	**FEL-I**	**FEL-II**
Wavelength (nm)	100 - 40	40 - 10
Output power (GW)	2+	1+
Pulse duration (fs)	100-800	100-800
Bunch charge (nC)	0.33 - 1.0	
Usable bunch length (fs)	200 - 800	
Energy spread (uncorrelated)	$1x10^{-4}$	
Emitance, slice (mm-mrad)	1.2	

REFERENCES

[1] "The RF Injector for the FERMI @ Elettra Seeded X-ray FEL", S. M. Lidia, M. B. Danailov, G. Penco, M. Trovo, FEL2005, Stanford, August 2005.

[2] "Frequency Modulation Effects in the Photoinjector for the FERMI @ Elettra FEL", S. M. Lidia, M. B. Danailov, G. Penco, M. Trovo, W. S. Graves, FEL2005, Stanford, August 2005.

[3] "Optimization and modeling of the accelerator for the FERMI @ Elettra FEL", S. Di Mitri, M. Cornacchia, P. Craievich, P. Emma, D. Wang, A. Zholents, FEL2005, Stanford, August 2005.

[4] "Emittance growth due to short-range transverse wakefields in the FERMI Linac", P. Craievich, S. Di Mitri, J. Wu, FEL2005, Stanford, August 2005.

[5] "Electron beam diagnostic based on a short seeded FEL", W.S. Graves, F.O. Ilday, F. Kaertner, T. Zwart, M. Danailov, B. Diviacco, M. Ferianis, M. Marsi, S. Lidia, Z. Huang, FEL2005, Stanford, August 2005.

[6] "Present performance and future requirements of the RF plants for the FERMI project", G. D'Auria, M. Ferianis, M. Milloch, L. Doolittle, A. Ratti, T. Zwart, FEL2005, Stanford, August 2005.

[7] L.H. Yu, Phys. Rev. A, **44**, 5178 (1991).

[8] R. Bonifacio *et al.*, Nucl. Inst. Meth. A, **296**, 787 (1990).

[9] "Optimization Studies of the FERMI at ELETTRA FEL Design", G. De Ninno, B. Diviacco, W. Fawley, G. Penn, W. S. Graves, FEL2005, Stanford, August 2005.

[10] "Generation and distribution of stable timing signals to synchronize RF and lasers at the FERMI@Elettra FEL facility", M. Ferianis, F. Kaertner, F. O. Ilday, J. W. Kim, J.Chen, A. Winter, J. Staples, R. Willcox, FEL2005, Stanford, August 2005.

[11] "Fiber Stabilization by Optical Heterodyning Technique and Synchronization of Two Mode-Locked Lasers with Two CW Lines", J. W. Staples, R. Wilcox, FEL2005, Stanford, August 2005.

[12] "Integrated design of laser systems for a FEL user facility", M.B Danailov, F. Ö. Ilday, F. X. Kaertner, FEL2005, Stanford, August 2005.

[13] "Advanced electron beam diagnostics for the FERMI@Elettra FEL", M. Ferianis, P. Craievich, G. D'Auria, S. Di Mitri, P. Emma, W.B. Graves, M. Poggi, FEL2005, Stanford, August 2005.

Studies of microbunching instability in FERMI@ELETTRA linac caused by longitudinal space charge. Part 1

Microbunching instability and longitudinal space charge effect have been studied before in various cases, most recently in Ref. [1]. The essence of the problem is that density modulations on the beam due to shot noise or some other external source of modulation are amplified by the longitudinal space charge and beam compression in bunch compression chicanes. Simulation of the effect of microbunching with particle tracking codes such as Elegant [2] faces some difficulty, because tracking is limited to a relatively small number of macroparticles (compared to the actual number of electrons in the beam). This artificially increases the shot noise in the tracking beyond the level of that in the real beam. For example, here we calculate the shot noise for a beam with the peak current I_b=75 A that can be seen at wavelength λ:

$$b = \sqrt{\frac{2ec}{I_b \lambda}} \quad , \quad b = 3.57\text{x}10^{-4} \text{ at } \lambda = 10 \text{ micrometers},$$

where e is the electron charge and c is the speed of light, and compare it to what we call the numerical shot noise of a 6-picosecond long electron bunch (FWHM) with 10^6 macroparticles,:

$$b = \sqrt{\frac{6\times10^{-12}\, 2c}{N\lambda}} \quad , \quad b = 1.90\text{x}10^{-2} \text{ at } \lambda = 10 \text{ micrometers}$$

Numerical shot noise is approximately 50 times larger. This indicates that numerical studies of the microbunching instability must be performed with a "quite launch" of particles using special algorithms that allow reproduction of a "natural" shot noise even with smaller number of particles. This is particularly difficult when it is necessary to use as an input a distribution produced by some other particle tracking code.

While looking for a solution to the problem we have analyzed the microbunching instability using analytical tools described in Ref. [1]. For the following beam parameters: uncorrelated energy spread σ_E=3 keV, compression factor in the first bunch compressor (BC1) = 4, initial energy = 100 MeV, energy at BC1 = 220 MeV, linac length (from 100 MeV to 220 MeV) = 20 m, we calculate the spectral dependence of the gain of the microbunching instability as shown in Figure 1. Then we moved the bunch compressor to 130 MeV (following a recommendation from Z. Huang) and used a 5 m long linac and repeated the gain calculations. Figure 2 shows the gain for this case. Comparing Figure 1 and Figure 2 we conclude that locating BC1 at 130 MeV gives less gain for the instability. This can be explained by the fact that slippage effect in the chicane magnets is proportional to a product $R_{56}\sigma_E / E_0$, where R_{56} is the time-of-flight parameter for a chicane responsible for a bunch compression and E_0 is the equilibrium beam energy. Obviously, for a given compression, this product is almost two times larger for E_0=130 MeV, than for E_0=220 MeV. Thus, the instability is more "Landau damped" for a chicane at 130 MeV, which we adopted for subsequent calculations.

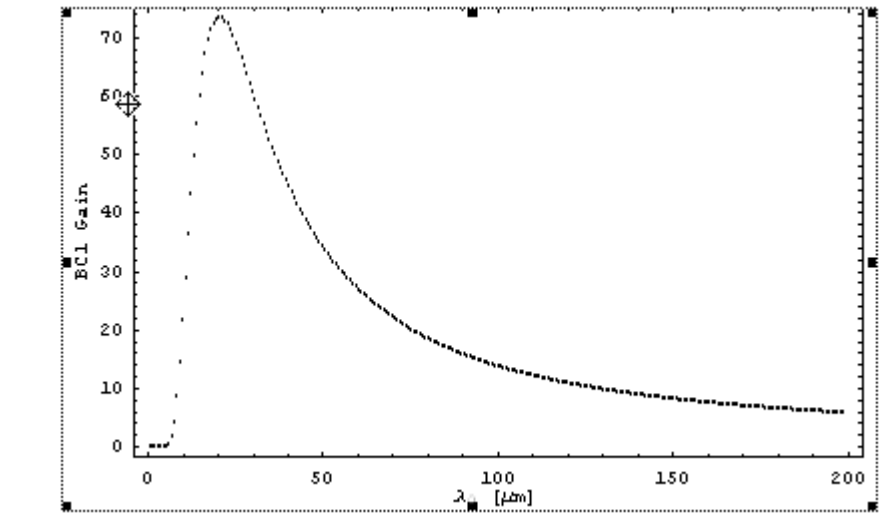

Figure 1. Gain of the microbunching instability after BC1 at 220 MeV

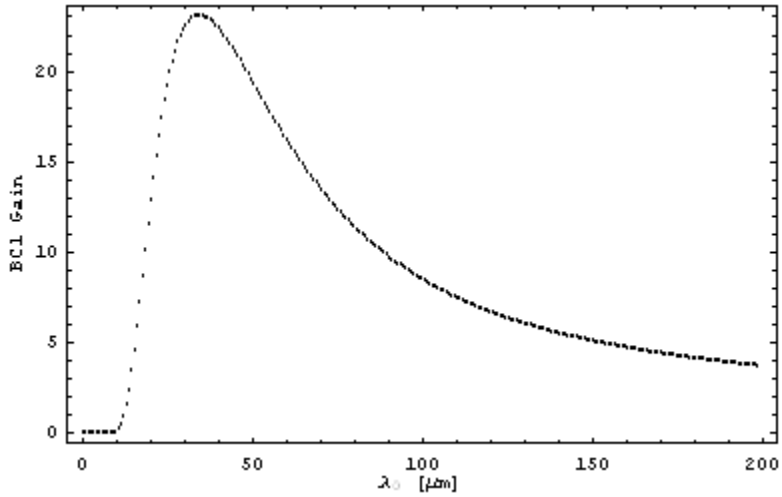

Figure 2. Gain of the microbunching instability after BC1 at 130 MeV.

Next we calculate the gain after the second bunch compressor using the following beam parameters: compression factor in the second bunch compressor (BC2) = 2.5, energy at BC2 = 600 MeV, linac length (from 130 MeV to 600 MeV) = 50 m, we calculate the spectral dependence of the gain of the microbunching instability as shown in Figure 3.

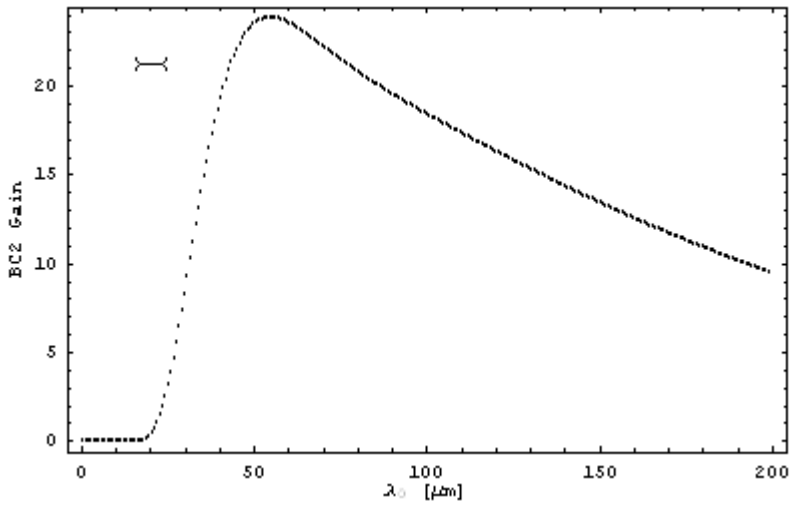

Figure 3. Gain of the microbunching instability after BC2 at 600 MeV.

At this point we also calculate the amplitude of energy modulation appearing on the electron beam as the result of the amplified shot noise. This is shown in Figure 4. In this calculation we also account for variation of the shot noise with the wavelength.

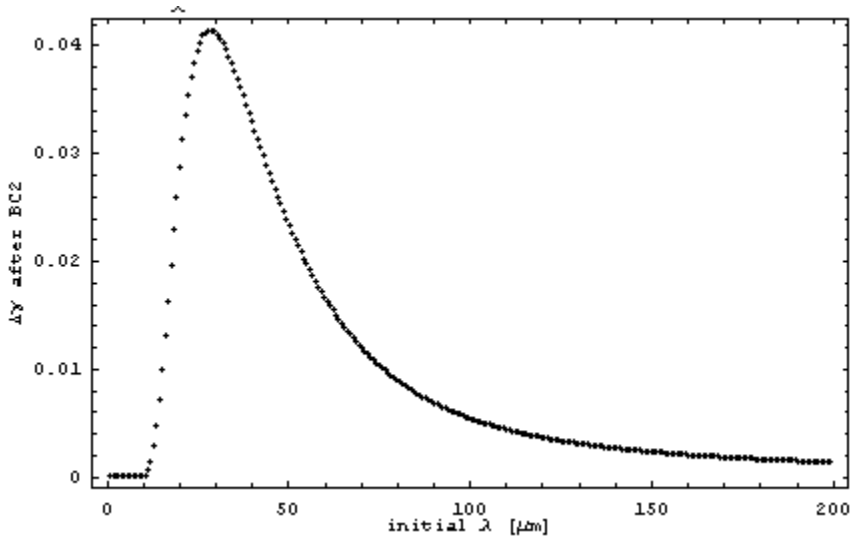

Figure 4. Spectral dependence of the energy modulation due to microbunching instability at the end of the BC2. Modulation grew out of shot noise.

Although the modulation does not look large at the peak, we note that in practice it must be even smaller, since the energy modulation with this amplitude will effectively de-bunch any density modulation on the beam at the peak wavelength. Figure 5 shows the efficiency of de-bunching (in relative units). Regions with over-bunching parameter greater than one qualitatively indicate wavelengths at which the instability comes to saturation, *i.e* when slippage caused by energy modulation is larger than a given wavelength.

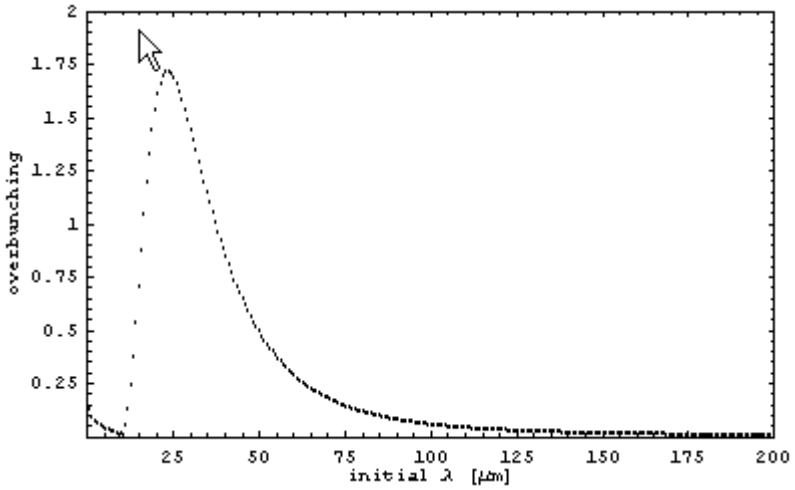

Figure 5. Over-bunching parameter as function of the wavelength for a nominal shot noise.

For comparison we plot in Figure 6 the energy modulation that we obtain if we use the numerical shot noise. The corresponding over-bunching parameter is shown in Figure 7.

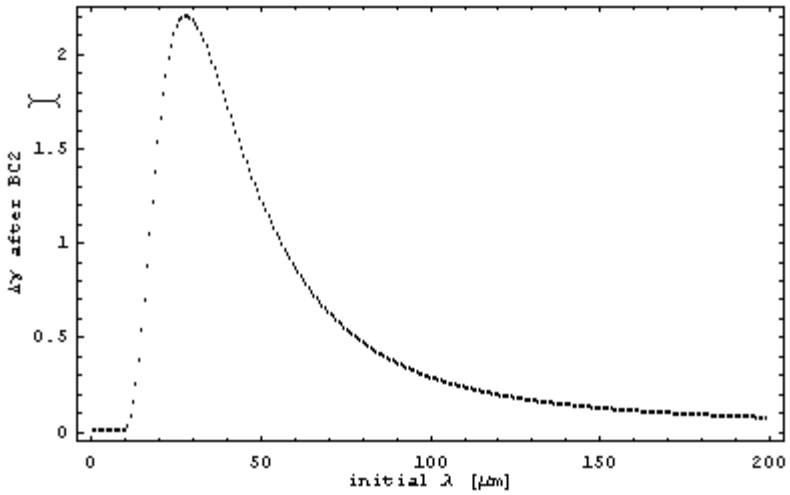

Figure 6. Spectral dependence of the energy modulation due to microbunching instability at the end of the BC2. Modulation grew out of numerical shot noise.

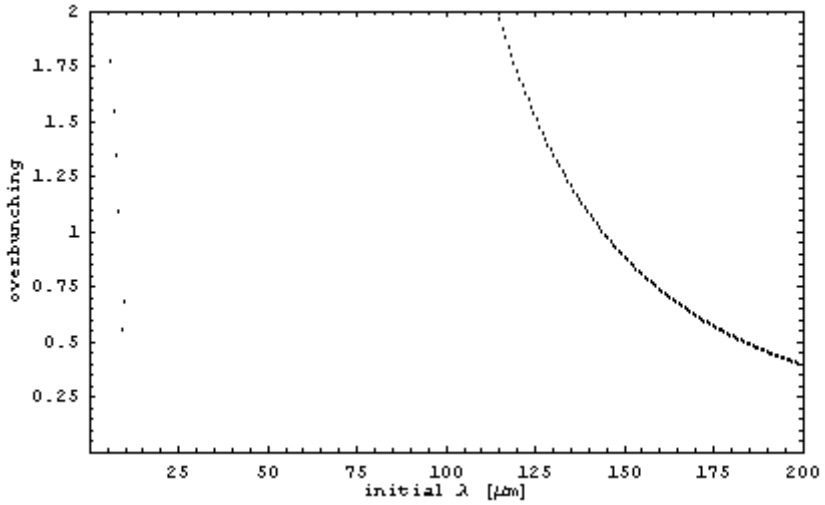

Figure 7. Over-bunching parameter as function of the wavelength for a numerical shot noise.

Here we see that the instability comes to saturation at all wavelengths below approximately 130 micron. This is in a good agreement with Elegant simulations where we observe microwave instabilities only above 110 microns.

Acknowledgement. Discussions with S. Di Mitri, Z. Huang and J. Wu were extremely helpful for understanding various details of the microbunching instability. Z. Huang also made available his Mathematica notebook.

References

[1]. Z. Huang *et al*., PRST-AB, 074401, 2004.
[2]. M. Borland,. APS LS-207, 2000.

Studies of microbunching instability in FERMI@ELETTRA linac caused by longitudinal space charge. Part 2

This note describes a continuation of the studies started in [1]

Energy modulation occurring prior BC2 creates spatial modulation after BC2. This contributes to the total gain of the microbunching instability after BC2 plotted in Figure 1.

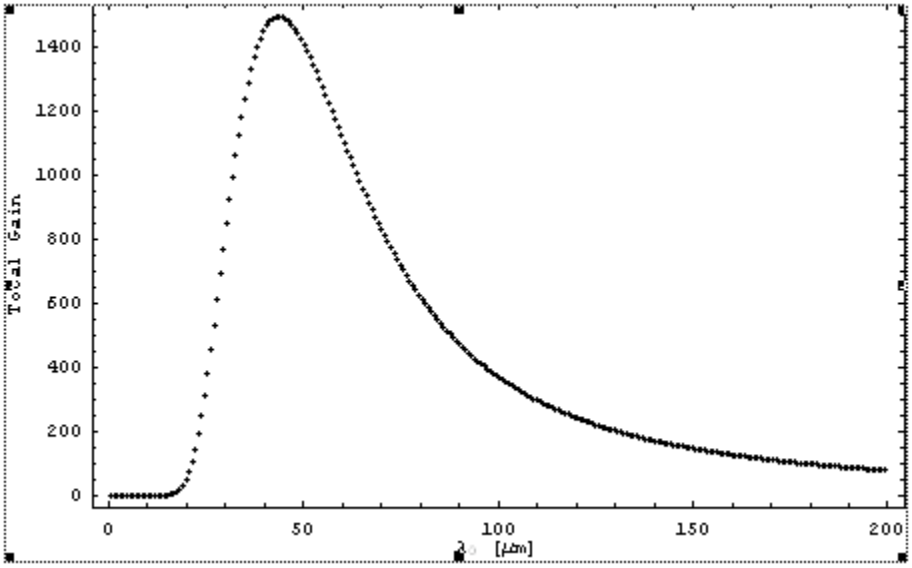

Figure 1. Spectral dependence of the total gain of the microbunching instability after BC2. Wavelength λ is referred to the initial beam *before* compression in BC1 and BC2.

When the electron beam passes approximately 40 m of the remaining linac after BC2 it gains additional energy modulation due to longitudinal space charge effects. The resulting total energy modulation at the end of the linac is shown in Figure 2. In computing this modulation we used real shot noise corresponding to 85 A peak current after the electron gun.

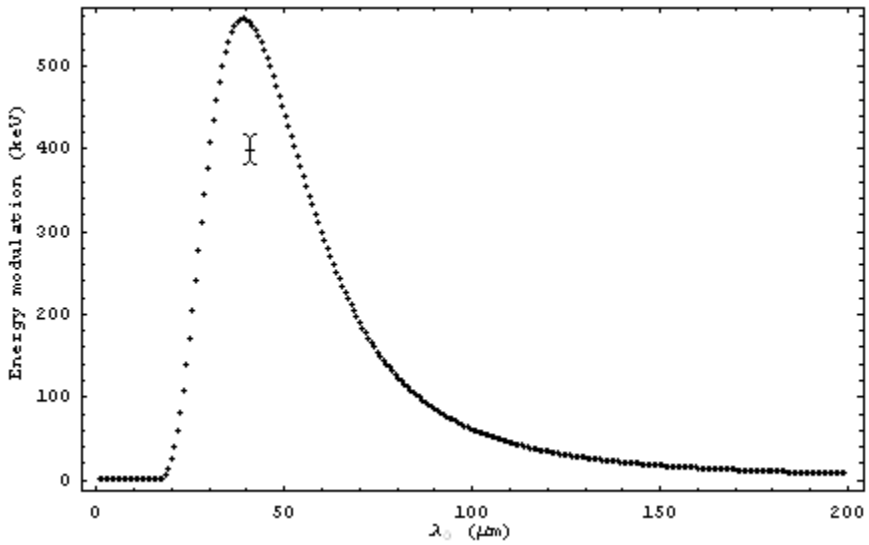

Figure 2. Energy modulation at the end of the linac due to the microbunching instability.

The above analysis shows that the most of the gain in the microbunching instability occurs after BC2, i.e. after transformation of the energy modulation to the spatial modulation that takes place in BC2. It is possible to avoid this if we use only one bunch compressor, BC1, for all our needs for bunch compression. There are also additional advantages in mitigation of the microbunching instability. First, we would need to increase R_{56} in BC1 (for a given energy chirp in the electron beam). Second, the relative energy spread is significantly larger at BC1 than at BC2. Both these factors would contribute to instability suppression due to increased "Landau damping" effect.

In order to test these ideas we performed the same analyses as described above using only BC1. We increased R_{56} from 7 cm to 8.4 cm and obtain a compression factor of 10 without changing the energy chirp of the electron beam prior to BC1. In Figure 3 we plot energy modulation due to the microbunching instability calculated at the end of the linac.

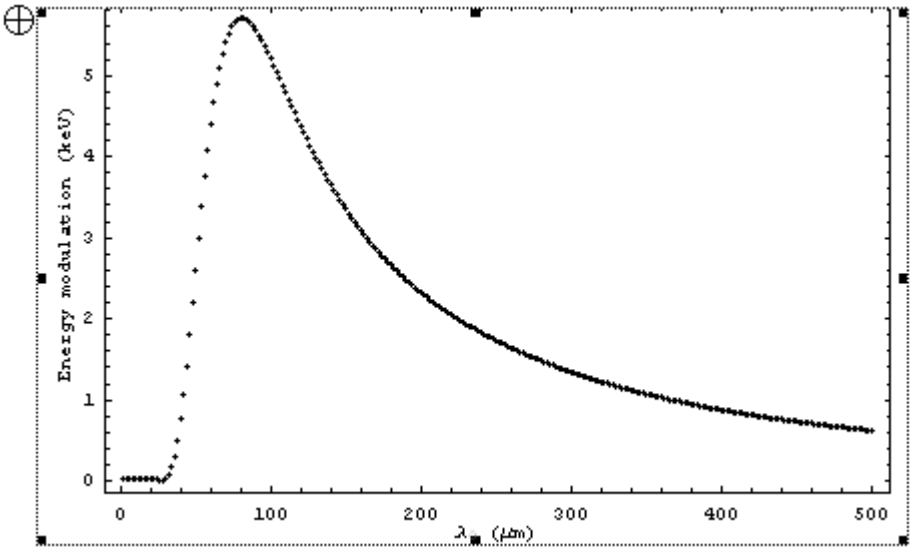

Figure 3. Energy modulation at the end of the linac due to the microbunching instability for a case of only one bunch compressor BC1.

Comparing Figure 2 and Figure 3 we find a significant reduction of the microbunching instability when all bunch compression is done at low energy, ~130 MeV. We recommend this scheme for further exploration by sensitivity studies to various jitters and by actual particle tracking using Elegant [2].

Then we calculate slice energy spread in the electron bunch assuming that the energy spread induced by microbunching instability will eventually become incoherent energy spread. In both cases, i.e. for two and one bunch compressors, we assumed an initial shot noise with a constant spectral power and calculated the rms energy spread induced in the beam by integrating over the entire spectra. In doing it we actually convolute spectra power density with spectral gain function $G(\lambda)$ calculated above:

$$\sigma_E^2 = \int \frac{db^2}{d\lambda} G(\lambda)^2 \, d\lambda$$

where *b* is the bunching defined in [1].

Finally we obtain $\sigma_E = 220$ keV for a case of two bunch compressors and $\sigma_E = 2.4$ keV for a case of one bunch compressor. This indicates that the microbunching instability is significantly smaller when all bunch compression is done with only one bunch compressor.

Acknowledgement. Discussions with M. Cornacchia, Z. Huang, S. Di Mitri and J. Wu were extremely helpful for understanding various details of the microbunching instability. Z. Huang had also made available for us his Mathematica notebook.

References

[1]. A. Zholents, CBP Tech Note-344, July, 2005.
[2]. M. Borland, APS LS-207, 2000.

Studies of microbunching instability in FERMI@ELETTRA linac caused by longitudinal space charge. Part 3

This is the final note related to a study of the microbunching instability initiated in [1] and continued in [2]. As was shown in [2], the microbunching instability creates excessive slice energy spread when two bunch compressors are used to get the final bunch length. Here we study means to reduce this energy spread.

The gain of the microbunching instability is very sensitive to the slice energy spread in the electron beam, *i.e*. uncorrelated energy spread. Typically, even a modest increase of the uncorrelated energy spread helps to damp the microbunching instability because of the "Landau damping" effect. It was proposed in [3] and then confirmed in [4] that a "laser heater" can be used as an efficient tool to provide an artificial increase of the uncorrelated energy spread. Here we analyze the effect of laser heater for FERMI@ELETTRA FEL project. In this analysis we simply assume that the laser heater provides some additional energy spread (specified for each particular case) and add this energy spread in quadrature to the initial beam energy spread.

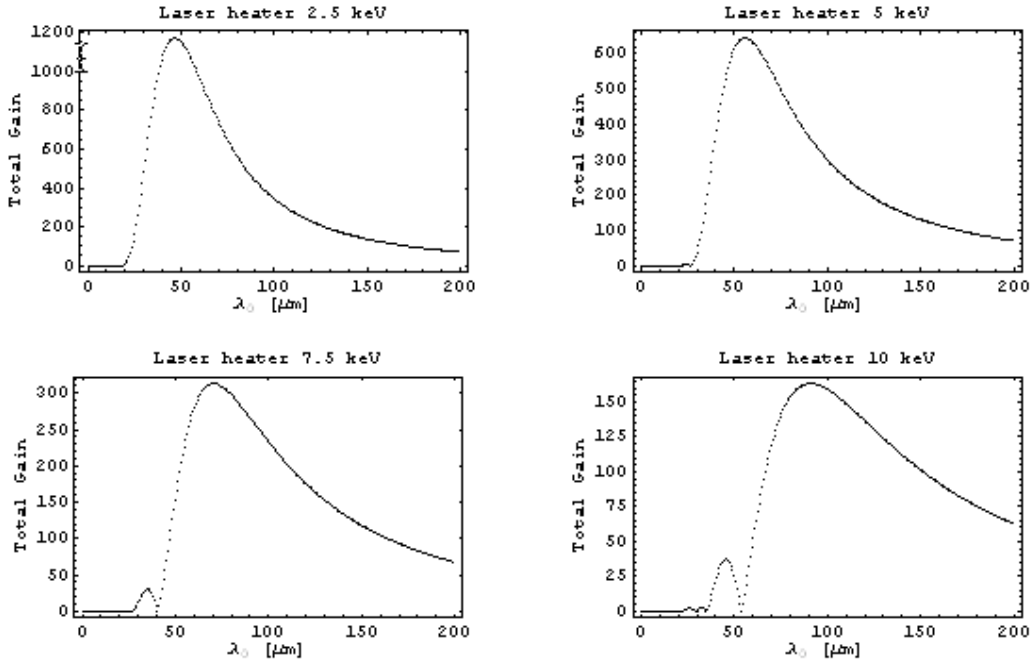

Figure 1. Spectral dependence of the total gain of the microbunching instability after BC2. Wavelength λ is the referred to the *initial* beam before compression in BC1 and BC2.

Figure 1 shows the gain of the microbunching instability calculated at the end of the linac for four cases with different magnitude of the uncorrelated energy spread added to the electron beam by the laser heater. The initial electron beam energy spread is 3 keV (see, also [1]). Clearly, the peak of the gain rapidly decreases with the increase of the energy spread provided by the laser heater and it is shifted to longer wavelengths where microbunching caused by particle density fluctuations due to shot noise is weaker.

By using the laser heater, we increase the slice energy spread, decrease the magnitude of the microbunching instability, and we expect to decrease the slice energy spread at the end of the linac. For example, adding 10 keV energy spread at the beginning of the linac produces at least 100 keV energy spread at the end of the linac when the overall compression factor in BC1 and BC2 is 10. In order to find the right magnitude of the "heating", we calculate the final energy spread at the end of the linac for various magnitudes of the laser heating and plotted the result in Figure 2. Here we find that by adding from 6 to 9 keV energy spread to the beam's initial 3 keV energy spread we would actually be able to reduce the slice energy spread at the end of the linac from 220 keV to approximately 70 keV.

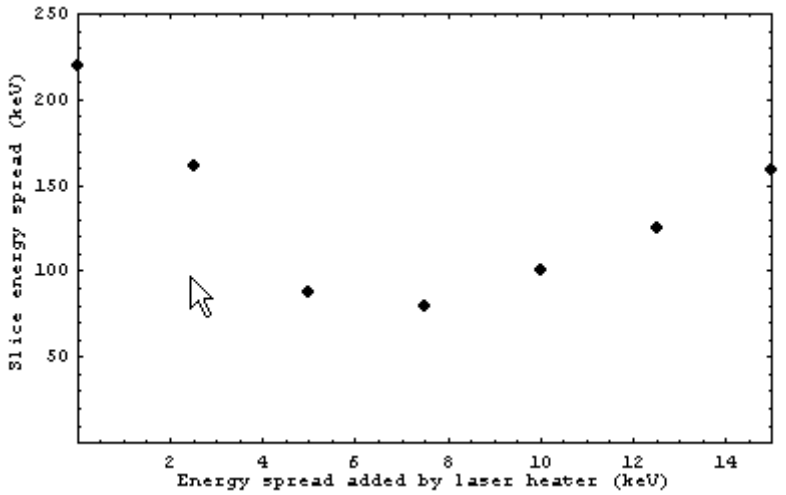

Figure 2. Slice energy spread at the end of the linac as a function of the magnitude of the artificially added energy spread using laser heater.

Next, we repeated the same calculations using computational noise instead of the real shot noise which is according to [1] stronger by an approximate factor of 50. This result is shown in Figure 3. Here we get slice energy spread of 240 keV when the laser heater is set to 15 keV. This is consistent with particle tracking using Elegant [5] showing 200 – 300 keV slice energy spread at the end of the linac when the laser heater is set to 15 keV. Moreover, we obtained significantly larger slice energy spread using a weaker laser heater, what is also qualitatively consistent with Elegant simulations. For example, with the laser heater set to 5 keV, we calculated 3.9 MeV slice energy spread.

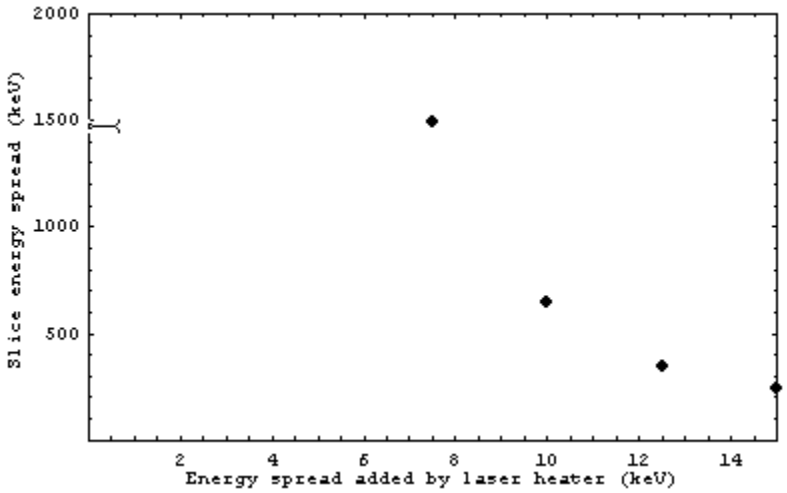

Figure 3. Slice energy spread at the end of the linac as a function of the magnitude of the artificially added energy spread using laser heater. Computational shot noise is used.

Acknowledgement. Discussions with M. Cornacchia, Z. Huang, S. Di Mitri and J. Wu were extremely helpful for understanding various details of the microbunching instability. Z. Huang had also made available for us his Mathematica notebook.

References

[1] A. Zholents, CBP Tech Note-344, July, 2005.
[2] A. Zholents, CBP Tech Note-345, July, 2005.
[3] E.L. Saldin, E.A. Schneidmiller, and M.V. Yrkov, DESY Report No. TESLA-FEL-2003-03, 2003.
[4] Z. Huang, *et. al*, Phys. Rev. ST –Acc. and Beams, V.7, 074401, (2004).
[5] M. Borland, APS LS-207, 2000.

Lattice between linac and FEL in FERMI@ELETTRA

Figures 1 shows beta and dispersion functions in the lattice between the linac and FEL-1. It consists of five sections: the *vertical ramp*, the *spreader* (both sections are marked on a drawing), *matching section one* between the linac and the vertical ramp, the *diagnostic section* between the vertical ramp and the spreader, and *matching section two* leading to FEL-1 after the spreader.

The *spreader* shifts FEL-1 aside by 2 m in the horizontal plane from the straight line leading to FEL-2. The spreader's lattice is practically identical to the lattice of the vertical ramp described in [1]. Similar to the vertical ramp, two bending magnets B5 and B6 provide a tilt to the electron beam trajectory in the horizontal plane with 12.5˚ angle which is compensated by bending magnets B7 and B8. The only difference between the spreader and the vertical ramp (besides bending in horizontal plane) is the distance between magnets B6 and B7, which is shorter than the distance between equivalent magnets B2 and B3 in the vertical ramp. This distance is chosen to provide 2 m offset for the beam trajectory (it is 5 m in the vertical ramp). R_{56} in the spreader can be adjusted and is currently set close to zero, *i.e.* the spreader lattice is practically isochronous. This is most beneficial when the electron beam has a large energy variation along the electron bunch as we may expect in our case. When tested with Elegant [2], the spreader lattice showed negligible emittance increase due to CSR for the same beam parameters as reported for the vertical ramp in [1].

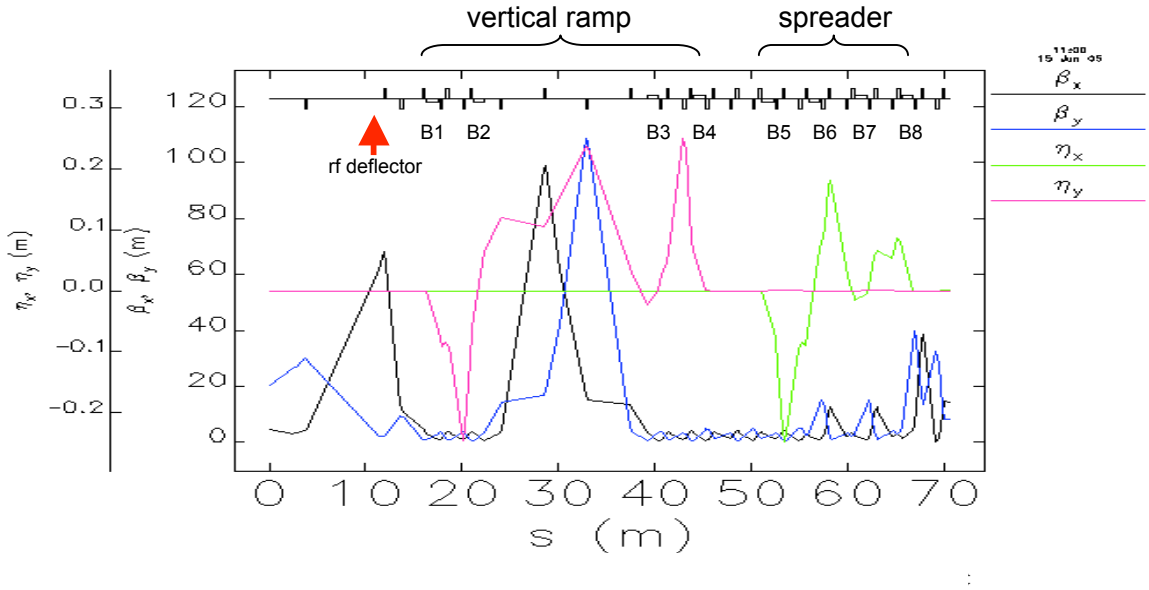

Figure 1. Twiss functions for a lattice between the linac and FEL-1.

The *matching section one* between the linac and the vertical ramp is designed with provisions for a time dependent beam diagnostic using an rf deflecting cavity and includes a region with a relatively large horizontal beta-function where this cavity can be placed. Presently we envision two types of measurements: measurement of the slice energy spread in a high dispersion point in the vertical ramp and measurement of the slice horizontal emittance in front of the beam dump at the end of the linac tunnel downstream from the first vertical ramp magnet B1.

We plan to measure the slice energy spread in the high vertical dispersion point [3]. This is located in front of the third quadrupole if one counts from after B1. Since we will measure the time variation of the vertical beam size, we need a deflecting rf cavity acting in the horizontal plane. For an accurate measurement we need a condition such that the energy related component to the total electron beam size dominates over the contribution from the beam emittance. In the operational lattice shown in Figure 1 we have vertical dispersion D_y= 0.25m and vertical beta function β_y= 3.7m. This means that for a slice energy spread $\sigma_E = 10^{-4}$ and a normalized emittance of 1.5 micron, we can only have the ratio of the energy related beam size to the betatron beam size equal to 0.6. This may not be sufficient. Therefore, for measurement with better precision we propose to use a modified lattice where this ratio is increased. Figure 2 shows a possible modification where we switched off two quadrupoles after B1 (as indicated on the drawing) and slightly tweaked other quadrupoles leading to B1. By doing this we obtain D_y= 0.34m and β_y= 0.9m resulting in the ratio of energy related beam size to the betatron size of 1.7. Two more provisions are also realized in the modified lattice. The betatron phase advance from the rf deflecting cavity to the slice energy monitor is made to be close to π/2 and the horizontal beta-function at the monitor location is increased to 7.5 m. Both these factors help to reduce the required rf deflecting voltage.

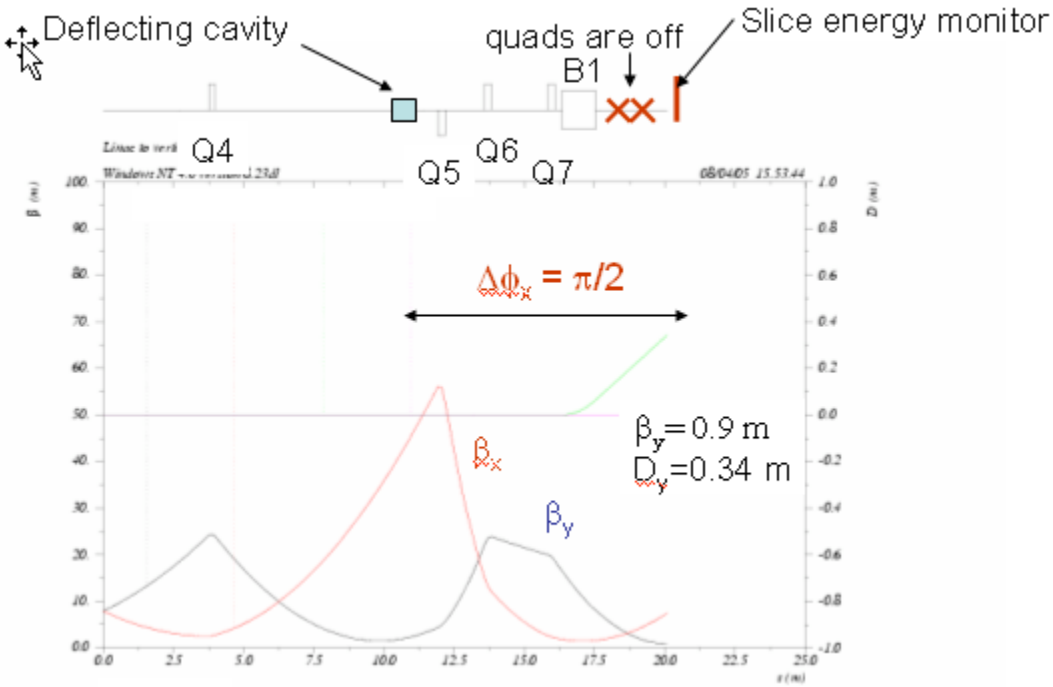

Figure 2. Twiss functions of the lattice modified for measurements of the slice energy spread.

The RF deflecting cavity acting in the horizontal plane can also be used for a measurement of the vertical slice emittance in the dispersion free region. This measurement can be done at the end of the linac tunnel and downstream from B1 just before the beam enters the dump. When B1 is switched off, no dispersion is excited. In order to obtain a betatron phase advance between the rf deflecting cavity and the monitor close to π/2 we propose to use

additional quadrupole after B1 and switch off the quadrupole before B1. Twiss functions for this variant of the lattice are shown in Figure 3. There, switched off elements are also indicated.

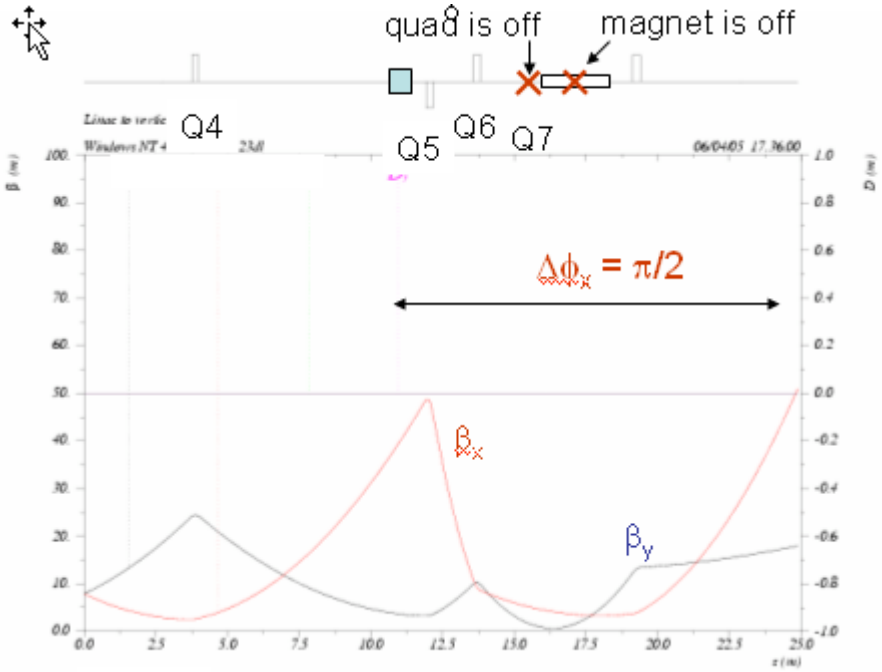

Figure 3. Twiss functions of the lattice modified for measurements of the slice vertical emittance.

The *diagnostic section* after the vertical ramp (see Figure 1) is envisioned for beam profile measurements in three locations with evenly increased phase advance in steps of ~π/4. It is designed as a standard FODO channel. Because of the limited space available after the vertical ramp, we were unable to make large beta-functions that otherwise would be useful for higher resolution in the beam profile measurements. Current length of this section is 7.2m and beta-functions at the location of the monitors are $\beta_x \approx \beta_y \approx 2$m.

The *matching section two* leading to FEL-1 after the spreader has four quadrupoles that are used to match the Twiss functions at the end of the spreader to the Twiss functions at the entrance of the FEL-1. Having four quadrupoles in this section allows reasonable flexibility in matching if either Twiss function is to be changed later.

References

[1] A. Zholents, The electron beam lattice for a vertical ramp in FERMI FEL, CBP Tech Note-334
[2] M.Borland, APS LS-207, 2000.
[3] P. Emma, private comunication.

Sensitivity of the bunch length to the phase jitter for the case of only one bunch compressor

According to [1] the variation of the compressed bunch length with phase jitter in the case of only one bunch compressor proposed for FERMI@ELETTRA in [2] can be calculated using the following formulae:

$$\frac{\Lambda\sigma_z}{\sigma_z} = \left(\frac{\sigma_{zi}}{\sigma_{zf}} - 1\right)\Lambda\varphi\,\mathrm{Cot}(\varphi_0)$$

where σ_{zi}, σ_{zf} are bunch lengths before and after compression, $\Delta\varphi$ is the phase jitter, and φ_o is the nominal phase (crest at φ_o=0). Figure 1 shows the result of calculation for various nominal phases assuming jitter of $\Delta\varphi$=0.1°, i.e ~100 fs timing jitter for S-band linear accelerator.

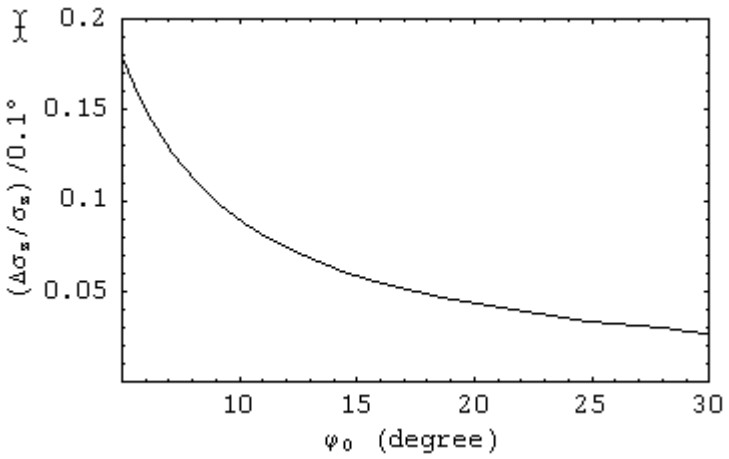

Figure 1. Variation of the bunch length as a function of the nominal phase for a phase jitter of 0.1°.

The magnitude of the bunch length variation for a larger phase jitter can be found by scaling the numbers shown in Figure 1.

We recommend to use φ_o>20°, where we do not expect any significant problem in the FEL due to fluctuation of the electron peak current associated with the bunch length variations due to the phase jitter.

References

[1] K.L. Bane *et al*, Proceedings PAC93, Washington DC, 1993.
[2] A. Zholents, CBP Tech Note-345, July 2005.

FERMI@Elettra Photoinjector and Diagnostic Beamline Design and Layout

Introduction

This technical note is to serve as a starting point for discussions between the various working groups that will define the components, layout, and operations of the FERMI@Elettra photoinjector. The initial layout of the photoinjector and diagnostic beamline under proposal for consideration is presented in Figure 1. The low energy transport line from the rf gun to the entrance of the first booster linac (S0A) is instrumented to allow two modes of operation: direct transport ("in-line") and deflection to an energy analyzing branch beamline. Two horizontal and vertical dipole correctors (Trim) and two BPMs are positioned to allow for trajectory corrections. A single magnetic quadrupole is included in the direct transport beamline to compensate for any residual phase-induced quadrupole field components in the rf gun or linac coupling cells that may interfere with emittance compensation. Standard in-line and interceptive diagnostics provide information on bunch current, transverse distribution and emittance. An energy analyzer comprised of a 90° bend and three quadrupoles will be used to measure the beam energy and energy spread. Deploying a streak camera to the end of the energy analyzer beamline may allow for detailed study of the beam longitudinal phase space profile.

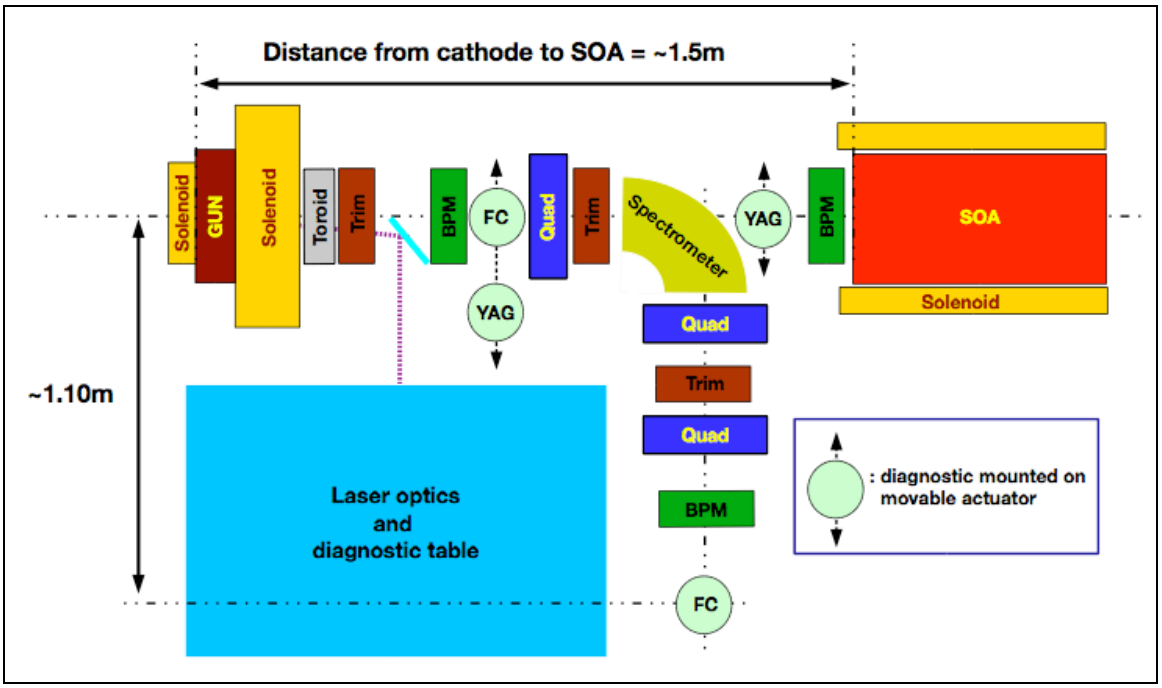

Figure 1: Photoinjector and energy analyzer beamline.

RF gun and in-line transport optics

The in-line beamline is defined as the transport line which connects the output flange of the rf gun with the entrance to the booster accelerator (S0A, S0B) and subsequent linac sections. The current (August 2005) physics model of the beamline assumes somewhat idealized field profiles for the beamline elements. The electron beam distribution, rf gun and linac cavity modes, solenoid magnet fields, and the resulting beam dynamics are assumed to be axisymmetric. In this approximation, no additional beamline elements are required to generate the high-brightness electron bunches and propagate them between the gun and booster linac.

The current physics model uses a simplified, free space model of the solenoid magnets. The resulting field distribution has a fairly long longitudinal reach that may likely interfere with downstream diagnostic performance. The emittance compensating solenoid will require a detailed design to include the influence of flux clamps, while maintaining the requisite solenoid field integral. Along with this, a companion bucking solenoid will be designed and included to null the on-axis magnetic field at the cathode plane.

A subsequent design for the basic beamline elements will include the following details:

- Emittance compensating solenoid with ferromagnetic field clamps, and bucking coil,
- Multiple modes for the rf gun ('zero' and 'pi' modes for the two-cell cavity),
- Dipole or quadrupole field (or impulse) components localized to the coupling cells in the rf gun and booster linacs,
- Trim dipoles to correct for misalignments and rf dipole induced deflections,
- Magnetic quadrupole to correct rf-induced quadrupole-symmetry impulses in rf coupling cells.

Diagnostic components

Beam properties to be measured directly

The photoinjector beamline will require several types of diagnostic to perform accurate and adequate measurements on the electron beam produced by the rf gun and photoinjector laser. These measurements include: (i) bunch charge and photocathode quantum efficiency, (ii) transverse beam position, (iii) beam energy and energy spread, (iv) transverse beam profile, and (v) thermal emittance. Only the bunch charge and transverse beam position measurements may be performed with non-interceptive diagnostics. All others will require interception and/or beam deflection.

Additional diagnostic measurements will be performed on the photoinjector laser pulse, which will be described elsewhere. Of particular interest to the operation of the photoinjector will be the laser spot size and transverse distribution on the photocathode, and the total pulse energy deposited on the photocathode. These may be inferred from optical diagnostics (virtual cathode and camera, laser pulse joulemeter, etc.) located in close proximity to the rf gun. Information on the longitudinal laser pulse distribution may be inferred from analysis on the optical spectrum, or by direct measurement with a streak camera.

Beam current and bunch charge will be closely monitored during commissioning and operation to detect any slow drift in the photocathode quantum efficiency (Q.E.). Charge variations will then be communicated to the photocathode drive laser in order to correct the emitted charge by altering the laser intensity. Larger charge variations may signal large changes in the average photocathode Q.E. which will then require more extensive corrective procedures, possibly including exchange with a new or reconditioned photocathode. Producing a very small spot size at the cathode, and measuring the photo current, one may then produce a map of the photocathode Q.E. over the region of interest.

Summary of standard in-line diagnostic elements

The standard complement of diagnostics will be employed on the in-line beamline. Bunch charge will be inferred from current measurements using an inductive toroid and an interceptive Faraday cup (FC). The difference signals from capacitive-button-type beam position monitors (BPMs) will provide measurement of the bunch charge-centroid position, while the summation signals may also be used to measure the bunch charge after calibration. For determination of the photocathode quantum efficiency the drop-in Faraday cup will provide the most accurate measurement of the bunch charge.

YAG-coated scintillator screens, which generate optical transition radiation (OTR) when the beam passes through, will be the primary diagnostic for transverse electron beam size and distribution. Paired with a quadrupole magnet upstream, the transverse emittance of the beam may be measured determined by scanning the quadrupole magnet gradient. At low bunch charges, the thermal emittance of the photocathode may also be measured in this way.

Standard diagnostic resolution and sensitivity

The electron beam during operations will carry a charge between 0.3-1.0 nC, with a bunch length of ~5ps (1.5mm), and a spot size diameter of several mm. The charge measurement diagnostics should then have a nominal resolution of ~10-50 pC under normal operations. Considering the size of the beam, sufficient position resolution is ~10-100 μm.

During commissioning and measurement of thermal emittances, the injector may be operated at reduced bunch charge levels, typically ~50 pC or less. For bunch charge measurement, it will then be necessary to deploy the Faraday cups on either beamline. These should maintain charge measurement resolution at less than 10 pC. The YAG-coated OTR screens have sufficient sensitivity at these lower bunch charge levels to provide gross spot size and trajectory measurements.

Beam properties that may be measured with an energy analyzer and a streak camera

A dispersive beamline that deflects the beam by 90° is used to perform measurements on the average beam energy and energy spread. The optics will be described later in this note. Single-shot streak-camera measurements of the Cherenkov or OTR light radiated by the final screen may be used to probe the longitudinal beam distribution and determine the longitudinal phase space emittance.

Beamline layout

The proposed beamline is shown in Figure 1. The in-line Faraday cup (FC) and OTR screens (YAG) are mounted on actuators to bring them in line with the beam, and then to be retracted after measurements are performed.

The required vacuum components are not indicated. At this time, it is assumed that a sufficient number of vacuum pumping ports will be supplied at the rf gun, at the laser window cross, and at the crosses containing the optical diagnostics and Faraday cups.

In-line transport line layout

The proposed layout of the in-line beamline is shown in Figure 2. The center positions of significant features along the beamline are indicated by numerals and described in Table 1. The table also lists the (assumed and most likely overly optimistic) longitudinal dimensions (i.e. the required beamline "real estate") of the various diagnostic elements. This will be a main topic for future discussions.

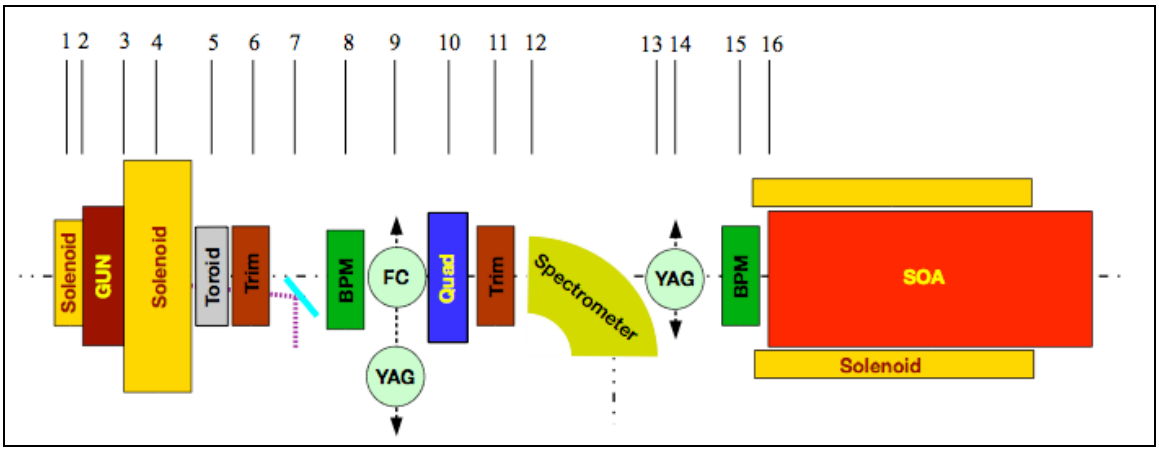

Figure 2: In-line beamline layout.

Diagnostic beamline layout

The diagnostic beamline layout is shown in Figure 3. The positions of significant features along the beamline are indicated by numerals and described in Table 2. This beamline is significantly less instrumented compared to the main, in-line beamline.

Table 1: In-line beamline features.

Feature #	Relative Midline Position [cm]	Longitudinal Length [cm]	Description
1	-5	5	Bucking coil
2	0	0	Photocathode plane
3	15	0	RF gun exit flange plane
4	19	10	Emittance-compensating solenoid
5	30	3	Current-monitoring toroid
6	35	5	Dipole trim coil
7	50	20	Laser mirror window
8	65	5	BPM
9	75	10	Faraday cup/OTR screen
10	95	5	Quadrupole (Q1)
11	105	5	Dipole trim coil
12	112.5	0	Dispersive bend entrance plane
13	127.5	0	Dispersive bend exit plane
14	135	10	OTR screen
15	145	5	BPM
16	150	0	S0A entrance

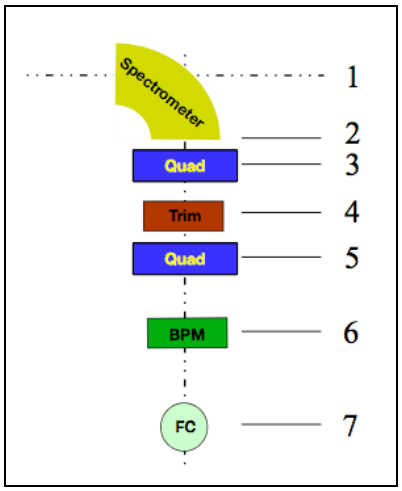

Figure 3: Diagnostic beamline layout.

Table 2: Diagnostic beamline features.

Feature #	Relative Midline Position [cm]	Longitudinal Length [cm]	Description
1	0	0	Centerline for In-line beamline
2	10	0	Dispersive bend exit plane
3	22.5	5	Quadrupole (Q2)
4	35	5	Dipole trim coil
5	47.5	5	Quadrupole (Q3)
6	75	5	BPM
7	105	0	Faraday cup/OTR screen entrance plane

Energy analyzer optics

To begin the modeling of the diagnostic beamline an electron bunch is generated at the cathode and transported for 89cm using ASTRA. At this point, the beam is several cm from the entrance to the first quadrupole in the energy analyzer. The distribution phase space is analyzed both for projected and slice-averaged Twiss parameters and emittances. These parameters are then passed to a MAD model to calculate the beam transport under finite dispersion, and to optimize the locations and strengths off the beamline elements.

The modeling and optimization of the energy analyzer beamline presented here is only a preliminary look to estimate the required field strengths and placement of the dispersive bend and quadrupoles. A future technical note will detail the physics design of this beamline and include estimates of the reasonably achievable energy resolution. Besides MAD and ELEGANT, simulations of the beamline using a fully three-dimensional space charge algorithm for very high aspect ratio beams will be necessary. A model using the Impact-T code as been created for this purpose, and will be used extensively.

Electron beam parameters

The electron beam horizontal and longitudinal phase spaces at the entrance to the energy analyzer (z = 89 cm) are shown in Figure 4. The beam has been decomposed into 200 longitudinal slices, and the slice emittance and Twiss parameters are shown in Figure 5. The emittances and Twiss parameters for both the projected distribution and the slice-averaged (weighted by the slice charge) beam are given in Table 3.

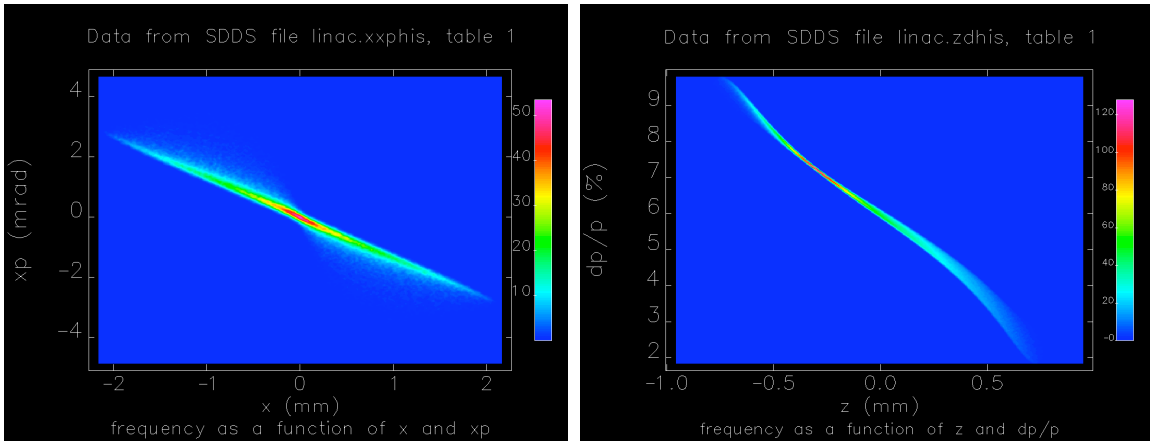

Figure 4: Electron beam horizontal (left) and longitudinal (right) phase spaces.

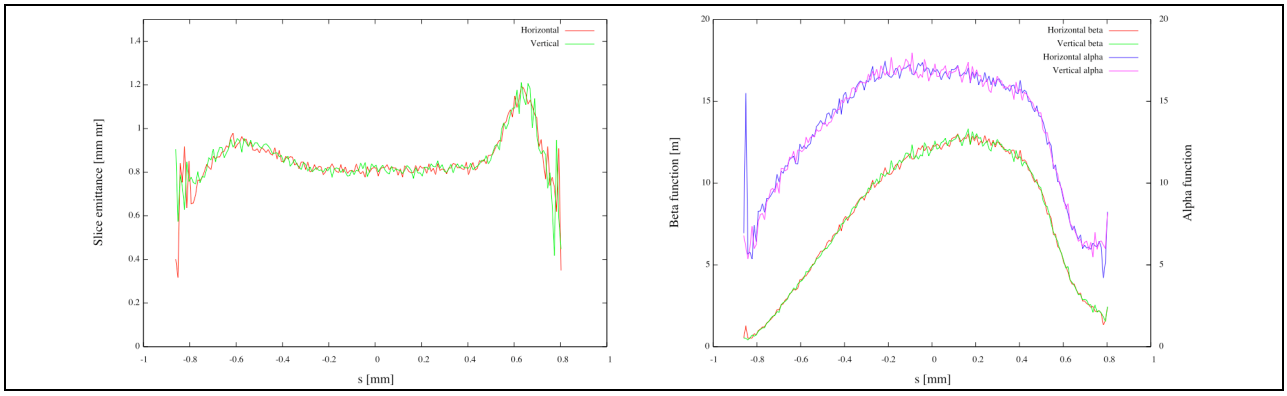

Figure 5: Beam slice parameters, emittance (left) and Twiss parameters (right).

Table 3: Beam Twiss parameter values at spectrometer entrance (89 cm from cathode).

Parameter	Projected	Slice-averaged
ε_x	4.075	0.855
β_x	1.935	9.422
α_x	3.097	14.91
ε_y	4.079	0.855
β_y	1.936	9.426
α_y	3.094	14.91

Electron beam transport through analyzer

The 90° bend magnet forces the beam onto a 10 cm radius of curvature orbit. The multiple quadrupole magnets are used to generate a finite value of the dispersion function at the end of the beamline while providing for point-to-point focusing. In this way, the energy resolution of the beamline may be maximized. The beam rigidity for 5.3 MeV electrons is $[B\rho]$ = 0.0186 T-m =18.6 kG-cm. The input deck for the MAD simulation is presented in the Appendix. The resulting optical functions are shown in Figure 6. The magnet strengths from the MAD model are listed in Table 4.

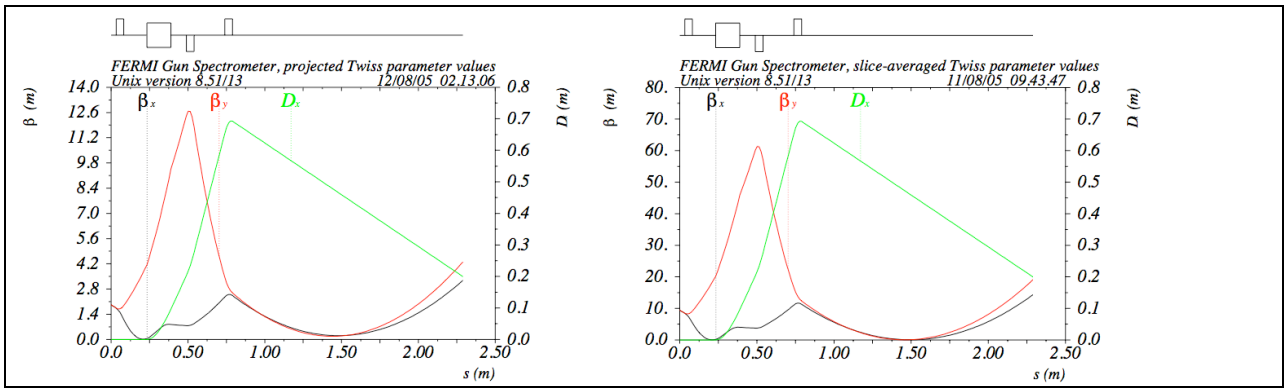

Figure 6: MAD models of energy analyzer showing the evolution of projected (left) and slice-averaged (right) Twiss parameters.

Table 4: Magnets for energy analyzer

Magnet	Bend angle (°) or Focusing strength, k (m^{-2})	Field Strength
Bend	90°	1.9 kG
Q1	80	1.5 T/m
Q2	-60	1.1 T/m
Q3	65	1.2 T/m

Conclusions

This note presents a proposed layout for the photoinjector beamline and a branch beamline for analyzing the energy, energy spread, and possibly the longitudinal phase space distribution of the low energy electron beam. The beamline presented here represents an initial compromise between the requirements of producing a high brightness electron beam, which tends to require shorter drift lengths between the rf gun and the first booster linac for proper emittance compensation, and the needs of the diagnostics and other instrumentation required to diagnose and to preserve the high quality of the beam. It is expected that further input from the injector physics, diagnostics and instrumentation, and project engineering personnel will be required to fully scope the capabilities and layout of the two beamlines presented here.

Appendix

MAD Input Deck

```
! FERMI@Elettra RF gun energy analyzer beamline
! Using slice-averaged Twiss values
! v.0.1 S.Lidia, 11 August 2005
!
TITLE, S="FERMI Gun Spectrometer, slice-averaged Twiss parameter values"
so : SEXTUPOL, L=0.10000, K2=27.32240 ! emulates solenoid
d0 : DRIFT, L=1.50000
d1 : DRIFT, L=0.03250
d2 : DRIFT, L=0.15000
d3 : DRIFT, L=0.10000
d4 : DRIFT, L=0.20000
d5 : DRIFT, L=1.50000
q1 : QUADRUPO, L=0.05000, K1=80.0
q2 : QUADRUPO, L=0.05000, K1=-60.0
q3 : QUADRUPO, L=0.05000, K1=65.0
! 90 degree bend has 10cm radius of curvature for 5.3MeV electrons
sp : SBEND, L=0.15710, ANGLE=1.5707963, K1=-0.00000, E1=0.100, &
       E2=0.100, HGAP=0.02000, FINT=0.5
RING: LINE = (d1, q1, d2, sp, d3, q2, d4, q3, d5)
USE, RING, SUPER=1
BEAM, EX = 0.855e-6, EY = 0.855e-6, sige=2.5e-2
INITIAL: BETA0, &
       BETX = 9.422, ALFX = 14.910, BETY = 9.426, ALFY = 14.911, &
       DX = 0.00000, DPX = 0.00000, DY = 0.00000, DPY = 0.00000
!Print characteristics of entire input beam line.
PRINT, FULL
TWISS,SAVE,BETA0=INITIAL
PLOT,table=twiss,haxis=s,vaxis1=betx,bety,vaxis2=dx,colour=100,spline
STOP
```

Initial Time-Dependent FEL Simulations

This reports an initial full time-dependent simulation of the FERMI FEL-1 device at an output wavelength of 40 nm using an ELEGANT-produced macroparticle distribution with longitudinal phase space of the electron bunch as shown below.

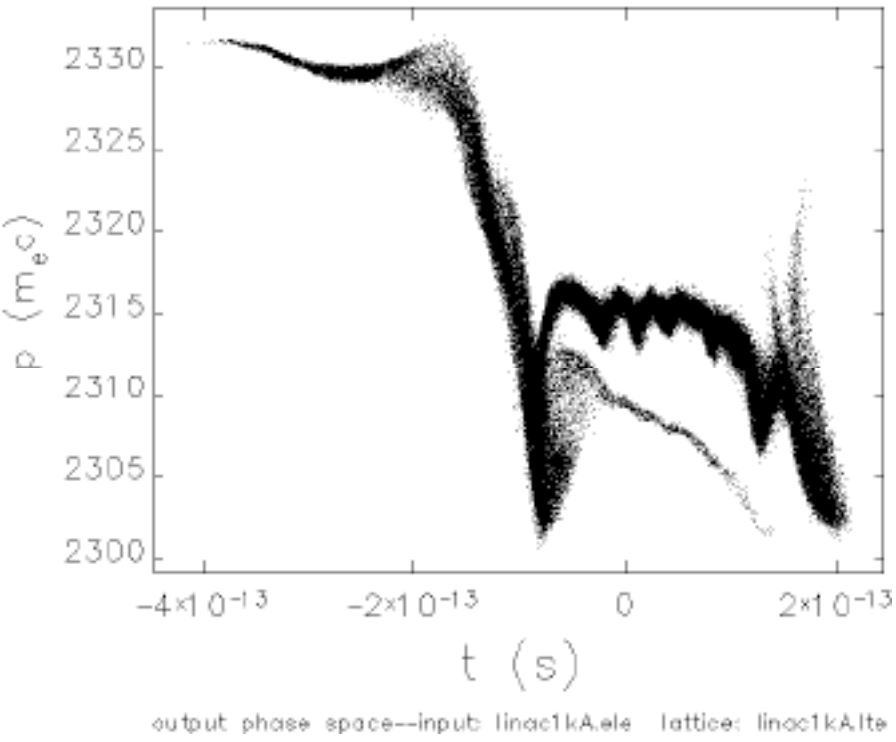

This particular run was with a beam charge of 0.3 pC and included effects from the longitudinal space charge instability. Inasmuch as the effective noise in the ELEGANT code (*vis-a-vis* this instability) is much higher than the theoretical shot noise value, the strong temporal oscillations in current and mean beam energy are not believed to be representative of the true situation. Nonetheless, it was felt to be extremely useful to do a time-dependent simulation with this distribution as it would help check out and debug any problems in the FEL codes when importing ELEGANT particle information. Over the "flat" portion of the bunch (i.e. where the current and energy are relatively constant), the average current was about 800 Amps and the mean energy corresponded to 1.185 GeV (see Figs. 1&2).

The input radiation seed power at λ=240 nm to the FEL-1 modulator was chosen to have the nominal value of 100 MW. The standard undulator, break length, quadrupole, and dispersive section lengths and settings were used as described in the table below. A total of 6 undulator sections were used in the 40-nm wavelength radiator.The "standard" ELEGANT macroparticle import capability of GINGER was used which effectively uses actual ELEGANT macroparticles to create the macroparticles in each longitudinal GINGER slice via an oversampling technique which preserves temporal correlations in the different phase space dimensions. 384 slices were followed in time with a 1.0-fs spacing together with 8192 particles/slice in a 16-fold symmetry

(before shot noise phase jitter was applied). The effective window in frequency space was +/- 1% which should more than sufficient to enclose the SASE gain bandwidth. The run was done with 32 processors on the NERSC IBM-SP and required well under 20 minutes.

FEL 1 (100-40 nm)

Parameter	Value	Units	*Last update*
Modulator FEL 1			
Type	Planar	-	*11 Mar 05*
Structure	One	segment	*11 Mar 05*
Period	16	cm	*11 Mar 05*
Period number	19	-	*11 Mar 05*
Length	3.04	m	*11 Mar 05*
Dispersive section			
Length	~ 1	m	*11 Mar 05*
R_{56}	~30 (@40 nm)	μm	*11 Mar 05*
Radiator FEL 1			
Type	Apple	-	*11 Mar 05*
Structure	4	segment	*11 Mar 05*
Period	6.5	cm	*11 Mar 05*
Period per segment	36	-	*11 Mar 05*
Segment Length	2.34	m	*11 Mar 05*
Break Length	1.04	m	*11 Mar 05*
Total Length	12.48	m	*11 Mar 05*
Optics FEL 1			
Type	FODO like	-	*11 Mar 05*
Quads strengths	±3.69	T/m	*11 Mar 05*
Quads lengths	19.5	cm	*11 Mar 05*
Resulting average β's	~10	m	*11 Mar 05*

Over the 384-fs time window, the average power grows at 40-nm wavelength to 800 MW, equivalent to 0.3 mJ in total pulse energy. The output radiation shows wide spectrum (see Fig. 4) and there is evidence of systematic chirping in the main body (Fig. 5) due to the input energy variations with time. The output pulse has and very limited longitudinal coherence as the normalized inverse bandwidth only reaches ~250 (Fig. 6) and the autocorrelation time (Fig. 7) is only 10-fs compared to >100-fs duration of the flat portion of the ebeam pulse. Since the input beam distribution was so compromised by the unphysical growth of the space charge instability, one should not put too much credence in the coherence results. Instead, one should note that the total output power is surprisingly large given the imperfect pulse.

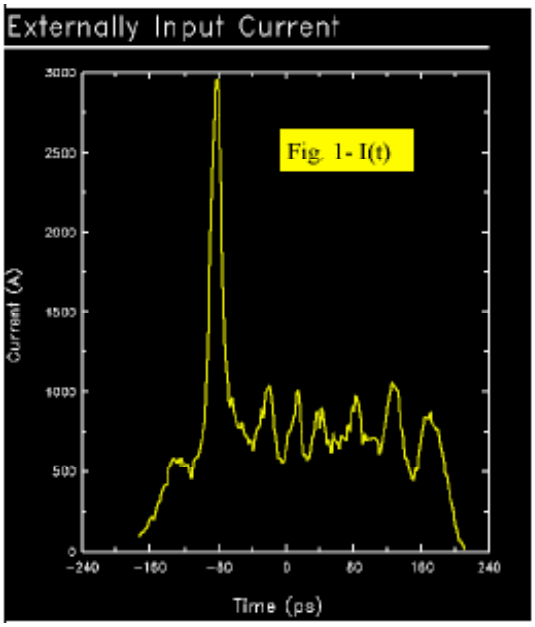
Externally Input Current
Fig. 1- I(t)
Current (A)
Time (ps)

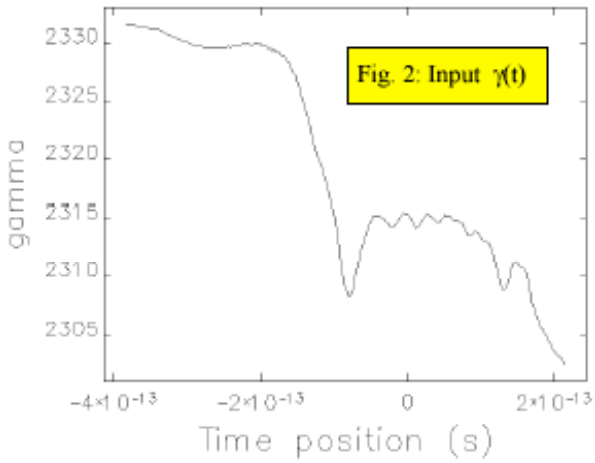
Fig. 2: Input γ(t)
gamma
Time position (s)

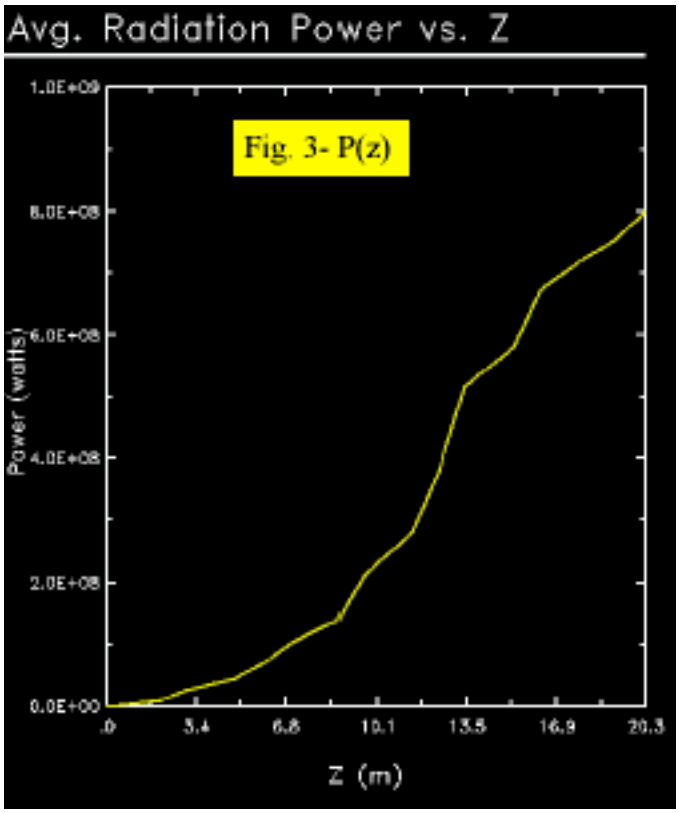
Avg. Radiation Power vs. Z
Fig. 3- P(z)
Power (watts)
Z (m)

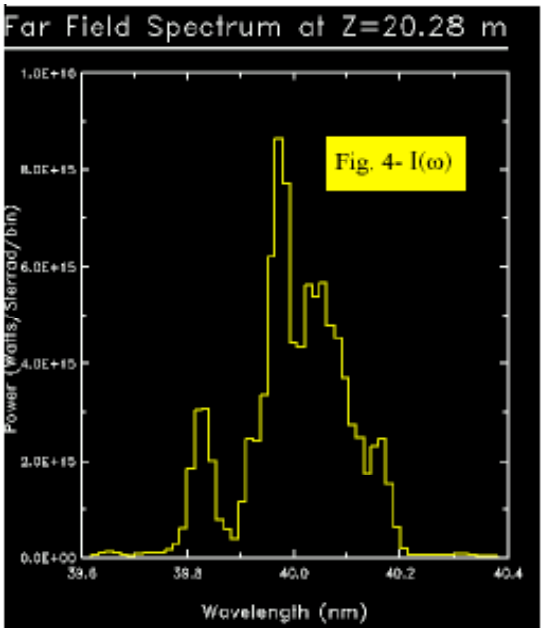

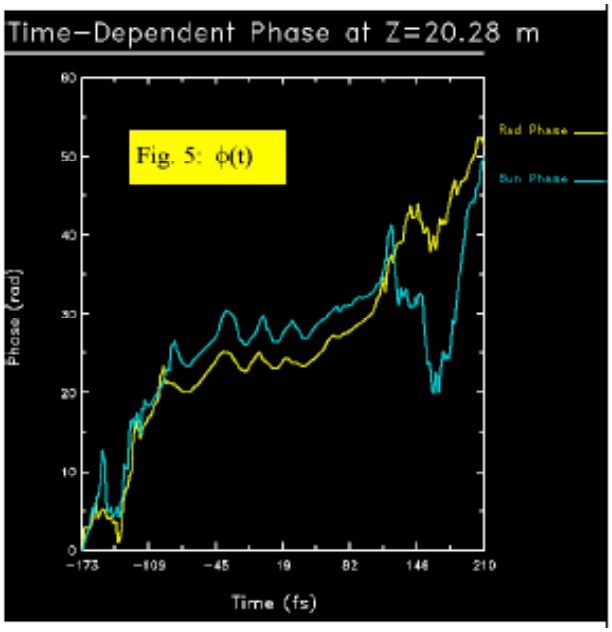

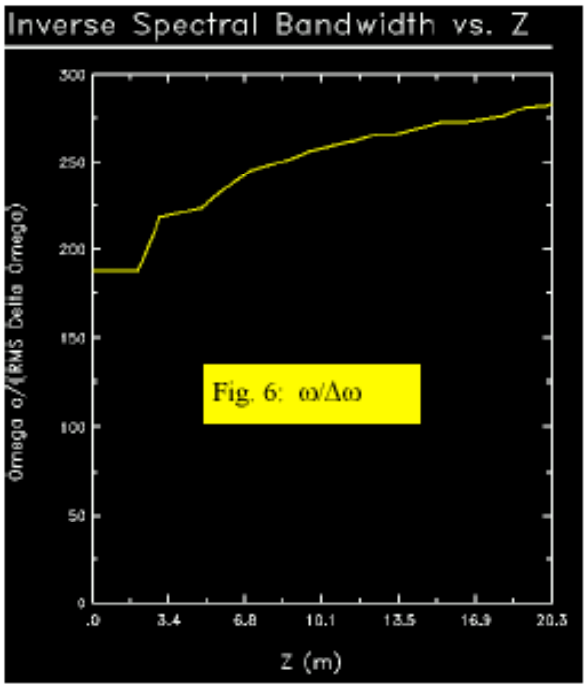

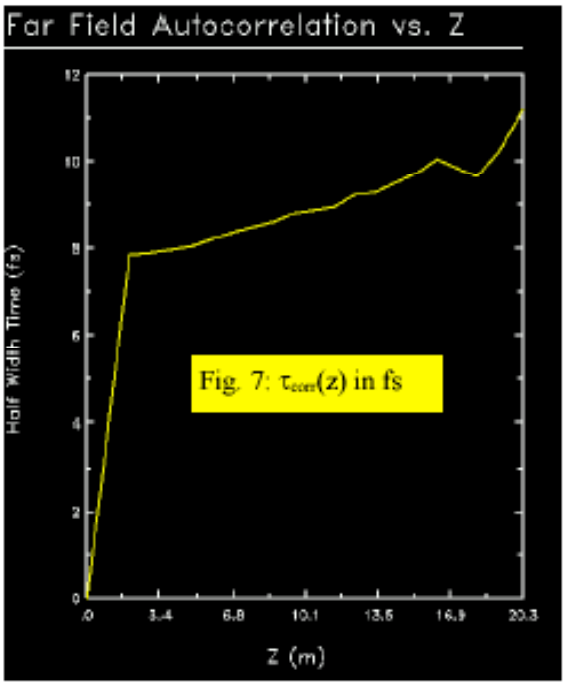

The simulation results are similar to those obtained with the GENESIS code. Figures 8, 9 show GENESIS output of time and frequency dependence for FEL-I at 40 nm.

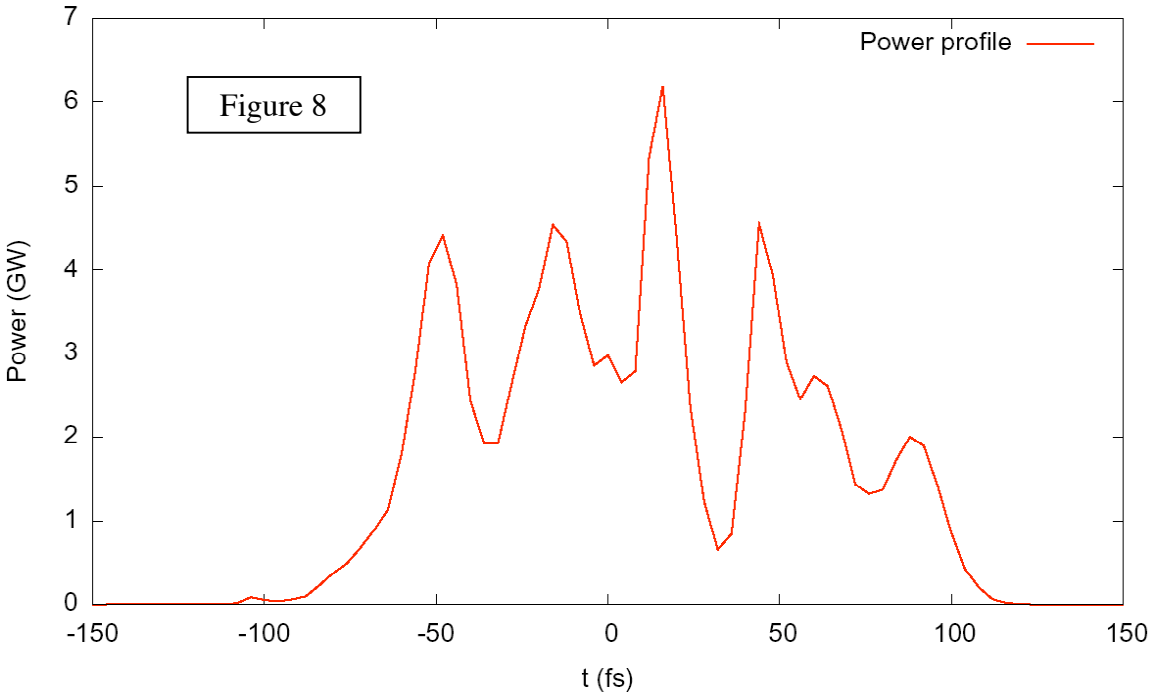

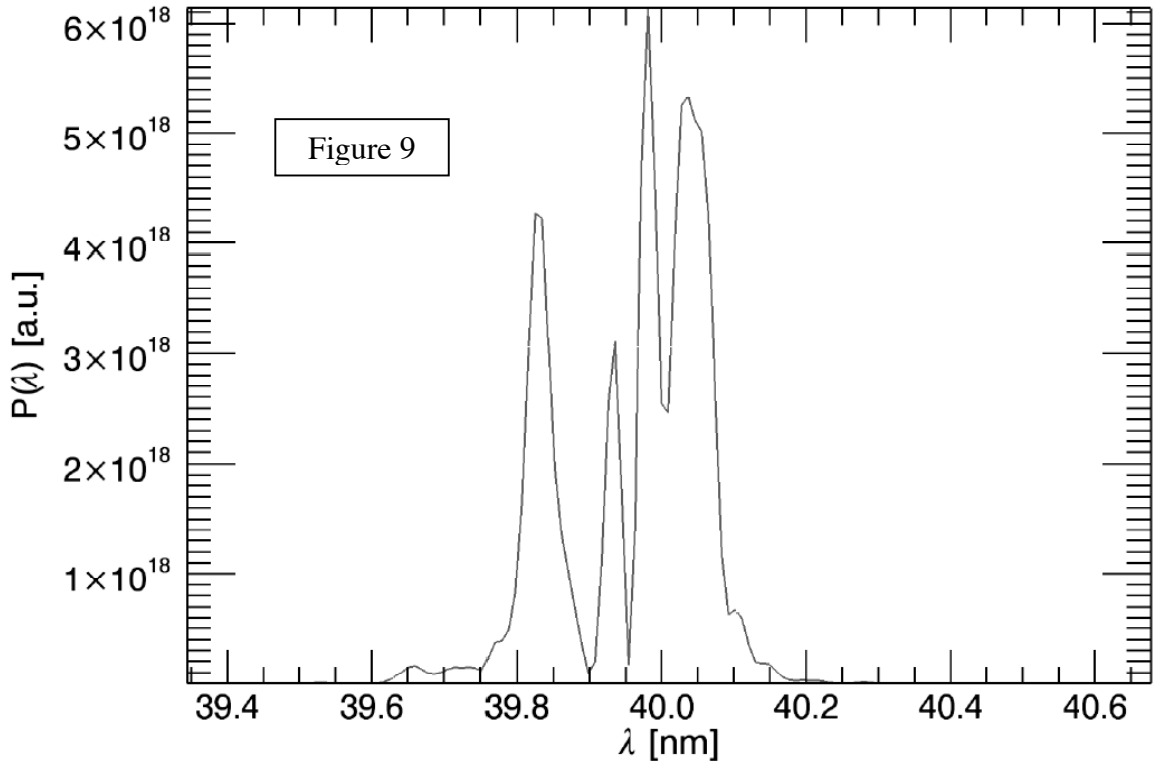

In addition, very preliminary GENESIS runs of FEL-II output are shown in Figures 10, 11. These figures show a summary of runs FEL-II at 10 nm. Tapering is included in Figure 11, but not for the model used in Figure 10.

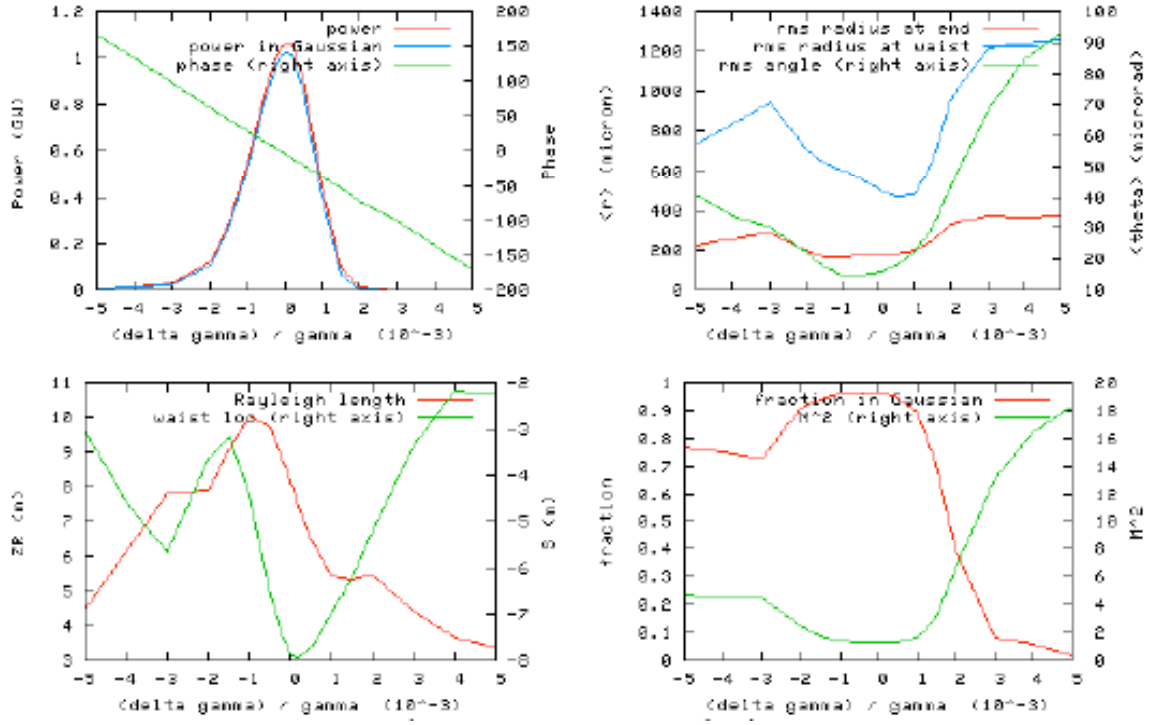

Figure 10 – FEL-II, 10 nm, no taper

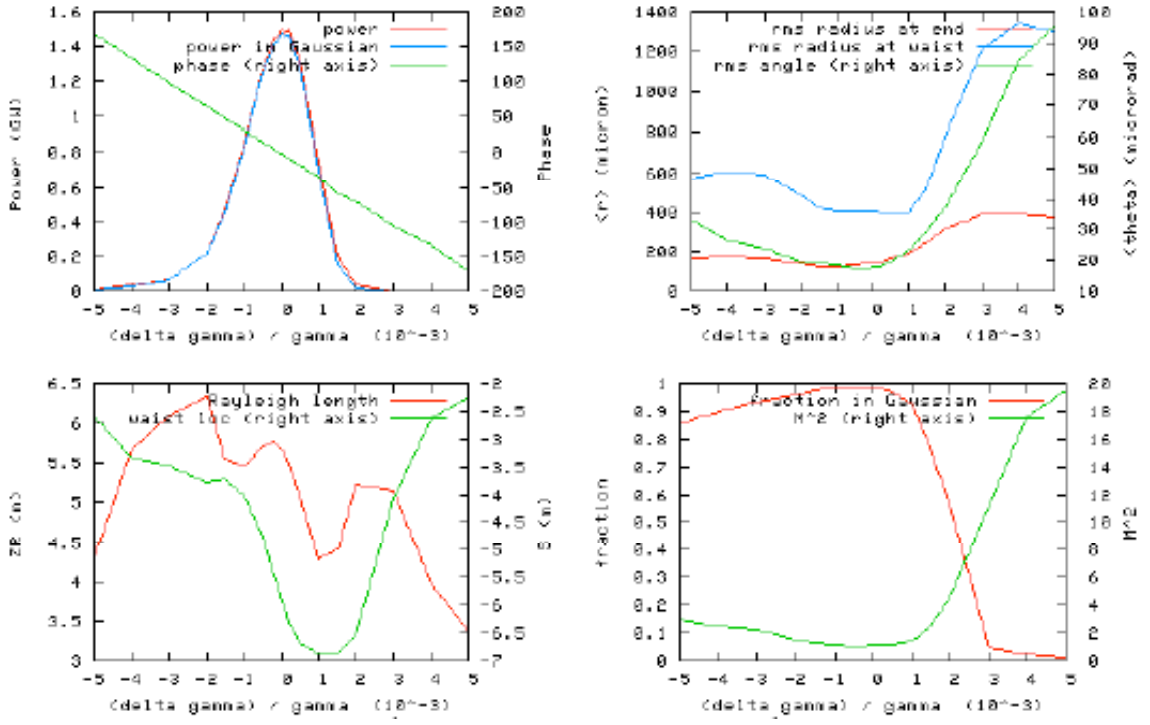

Figure 11, FEL-II, 10 nm, with taper